

Flares in Open Clusters with K2.

II. M35, Hyades, and Ruprecht 147

Ekaterina Ilin¹, Sarah J. Schmidt¹, Katja Poppenhäger¹, James R. A. Davenport² and Klaus G. Strassmeier¹

¹ Leibniz Institut für Astrophysik Potsdam

e-mail: eilin@aip.de

² University of Washington e-mail: jrad@uw.edu

Received XXX; accepted XXX

ABSTRACT

Context. Flares can help us trace magnetic activity because are bright and high-contrast on low mass stars.

Aims. This study aims to quantify flaring activity on these stars as a function of mass and age.

Methods. We automatically detected flares in K2 time-domain photometry, using the open-source software K2SC to remove instrumental and astrophysical variability from K2 light curves. We used injection and recovery of synthetic flares to assess detection thresholds, time sampling and de-trending effects on the inferred flare energies. With additional data from the full K2 archive we added stars with a larger variety of ages and spectral types to the analysis of the previous study (Ilin et al. 2019). We compared previous results from the Pleiades and Praesepe to the flare frequency distributions (FFDs) in M35 and the Hyades, respectively. Ruprecht 147 filled in the age gap at 2.5 Gyr between the aforementioned young clusters and the solar age cluster M67.

Results. We find that the flare production mechanism is similar for the entire parameter space, following a power law relation with exponent $\alpha \approx 2$, but the flaring frequencies depend on both mass, and age. We discuss X and Y.

Key words. Methods: data analysis, Stars: activity, Stars: flare, Stars: low-mass

Use \titlerunning to supply a shorter title and/or \authorrunning to supply a shorter list of authors.

1. Introduction

2. Data

Flares are explosion on stellar surfaces with a complex spatio-temporal and energetic phenomenology. We know that flares are magnetic re-connection events that lead to a change in field line topology and subsequent energy release (Priest & Forbes 2002). We can observe flares in nearly all electromagnetic bands, from radio to X-rays, and on all stars that possess a convection zone from late F type stars to ultracool dwarfs (Gizis 2013). But despite continuous monitoring in high temporal resolution, the random occurrence of flares makes them tricky to observe on the Sun, especially in coordinated multi-band observations. In integrated light, most flares have a far too low contrast and intensity to be observable. Stellar flares on cool stars have two advantages in this respect. They are often bright, enhancing stellar flux by up to several orders of magnitude, and they typically exhibit blackbody emission at temperatures significantly higher than their stars' photospheres.

With the evidence that the origins of flares on the Sun and other stars are the same (e.g., Tepke et al. 2016), solar and stellar flare scanning observational programs have been developed to search for flares on selected stars (e.g., Pawlakowicz et al. 2011; Stasińska et al. 2012; Clarke et al. 2018). Basic parameters that affect flaring behaviour on stars are their mass and age. Age studies in binaries showed consistency in activity for both compact (M35) and extended (M67) clusters (Semenov & Fomichev 2017; Jeet et al. 2015; Clarke et al. 2018). Open cluster mass - age relation based on FFDs was determined by Ilin et al. (2019) (hereafter Paper I) investigating the K2 data collected on the two-wheeled Kepler satellite, it was Ktonid-M dwarf stars in three open clusters (OCs), the Pleiades, Praesepe, and Ruprecht 147, subject to drift motion of the spacecraft relative to the flare frequency.

The present study aims to extend the results in Paper I to the age of Ruprecht 147 (the effects of high resolution were developed in previous study).

Our main data are K2 target pixel files that were provided by the Kepler archives hosted at MAST, and light curves derived from them (Aigrain et al. 2016; Soares-Furtado et al. 2017; Vinícius et al. 2018). To assign T_{eff} to the targeted stars we used multi-band photometry obtained from Tycho, UCAC4, 2MASS, Pan-STARRS, and Gaia catalogs. To assign ages to the targeted stars, OC membership information was compiled from the literature. An overview over the cluster sample is presented in Table ?? and illustrated in Figure 1.

2.1. K2 light curves

The Kepler (Koch et al. 2010) spacecraft finished its follow-up mission K2 (Howell et al. 2014) in September 2018, after having completed nearly 20 80-day observing campaigns. Even though Kepler and K2 data are used in more than 2 400 publications to date, the public archive can still be considered underutilized (Barentsen et al. 2018). In this spirit we took up the analysis of about 4 000 Kepler target pixel files that each contain up to 80 days of 30 min cadence observations in white light ($4, 200 - 9, 000 \text{ \AA}$). We also used digital images extracted from the Kepler superstampulations from the K2 data archive. These images are aggregated sets of typical Kepler data, corresponding to a specific field of view, placed generally densely on the flat field that also covered and flaring stars. The images were taken with a fixed exposure time of 10 s and a frame rate of 10 Hz. The images were processed with the K2 pipeline (Koch et al. 2010) and had an overall reduced pointing accuracy. To determine the effects of the high resolution we developed the previous study.

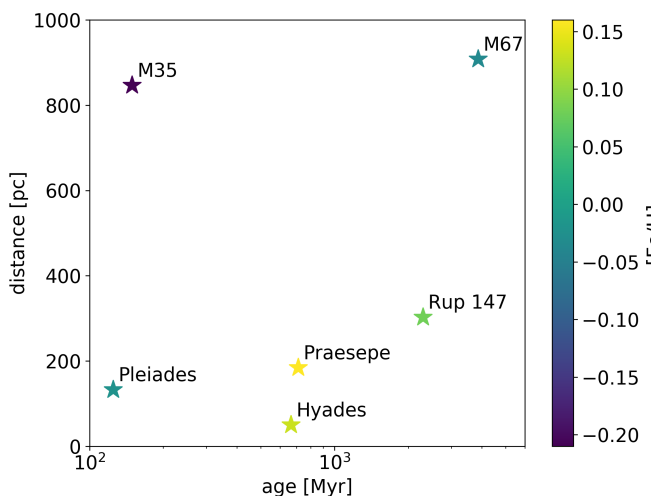


Fig. 1. The values for age, metallicity, and distance are approximate values from a compilation of existing literature, see Appendix B.1.

perI). We revisited the memberships from Rebull et al. (2016a), which were your in the previous work, and merged them with lists of members determined by Olivares et al. (2018); Gaia Collaboration et al. (2018a); and Cantat-Gaudin et al. (2018).

2.3.2. M35

M35 is a ZAMS cluster 900 pc away, observed during Campaign 0 in K2. We merged membership lists from Cantat-Gaudin et al. (2018); Gaia Collaboration et al. (2018a); and Bouy et al. (2015). There are only five K2 light curves, but we identified multiple additional members with publicly available¹ light curves obtained from Soares-Furtado et al. (2017). They used an image subtraction technique in the campaign’s super stamps, a self flat-fielding de-trending inspired by K2SFF (Vanderburg & Johnson 2014), and a trend-filtering algorithm developed by Kovács et al. (2005). We preferred PSF photometry in cases where both aperture K2 and PSF LCs were available. We took the raw extracted PSF light curves and de-trended them using K2SC.

derburg & Johnson 2014; Aigrain et al. 2016; ?; Luger et al. 2018)

32 **2.2. Membership matching**
 33 We obtained membership information from multiple catalogs
 34 for each cluster. We cross-matched these catalogs on RA and
 35 declination within 3 arcsec. The resulting target lists were
 36 used to search the K2 archive, or were matched to the catalogs
 37 of extracted light curves from crowded fields in the case
 38 M35 (Soares-Furtado et al. 2017) and M67 (Nardiello et al.
 39 2016).

40 One part of the membership catalogs provided membership
 41 probabilities (Douglas et al. 2014; Bouy et al. 2015; Canta
 42 Gaudin et al. 2018; Olivares et al. 2018; Reino et al. 2018; Ga
 43 2018; Olivares et al. 2019). For the other part no probabil
 44 was provided (Rebull et al. 2016a; Douglas et al. 2017; Ga
 45 Collaboration et al. 2018a), or qualitative classifiers were
 46 given (Curtis et al. 2013; Gonzalez 2016; Rebull et al. 2017). In
 47 the latter cases we assigned approximate probabilities anchored
 48 to the set threshold for inclusion into our final sample. Absence
 49 in a catalog did not decrease the likelihood of membership,
 50 each catalog shows different selection biases which we did not
 51 address in this study. We set the threshold mean membership
 52 probability p for a target in our sample to 0.8.

54 2.3. Open Clusters

55 We studied flaring activity in the low mass stars in six open
 56 clusters spanning from ZAMS to solar age. Table 1 provides an
 57 overview over the final sample. The literature overview of age
 58 distance, and metallicity determinations is given in Table ??, the
 59 Appendix. Membership probability histograms of the first
 60 sample are displayed in Figure ??.

61 2.3.1. Pleiades

62 The Pleiades, a nearby ZAMS cluster, were observed in Cam
 63 paign 4, and were treated in PaperI. We include the cluster in
 64 this work for completeness and to illustrate improvements to (Pa

83 2.3.3. Hyades

The Hyades are a 0.6 Gyr old OC observed during Campaigns 4 and 13 with K2. It is about as old as Praesepe. We merged membership tables obtained from Douglas et al. (2014); Reino et al. (2018); and Gaia Collaboration et al. (2018a).

2.3.4. Praesepe

Praesepe appeared in Campaign 5, and was previously treated in PaperI. It was then observed again during Campaign 13. We revisited the memberships obtained by Douglas et al. (2014), and matched them to the members identified in Douglas et al. (2017); Rebull et al. (2017); Cantat-Gaudin et al. (2018); and Gaia Collaboration et al. (2018a).

2.3.5. Ruprecht 147

Ruprecht 147 is a 2.5 Gyr old OC observed during Campaign 7 with K2. We used the mean membership probabilities obtained from a number of studies (Curtis et al. 2013; Cantat-Gaudin et al. 2018; Olivares et al. 2019) combined with the members found by Gaia Collaboration et al. (2018a) to identify the most likely members.

2.3.6. M67

M67 is a solar-age, solar metallicity OC about 900 pc away. Multiple members were observed during Campaign 5, and revisited in Campaigns 16 and 18. We did not find any flares in M67 in Campaign 5 (PaperI) observing the members identified by Gonzalez (2016). The recent campaigns brought both additional observations, and entirely new targets to the sample. We merged the members from Gonzalez (2016) with a recent study based of Gaia DR2 data (Gao 2018). Additionally, we obtained PSF-detrended light curves for Campaign 5 from Nardiello et al. (2016).

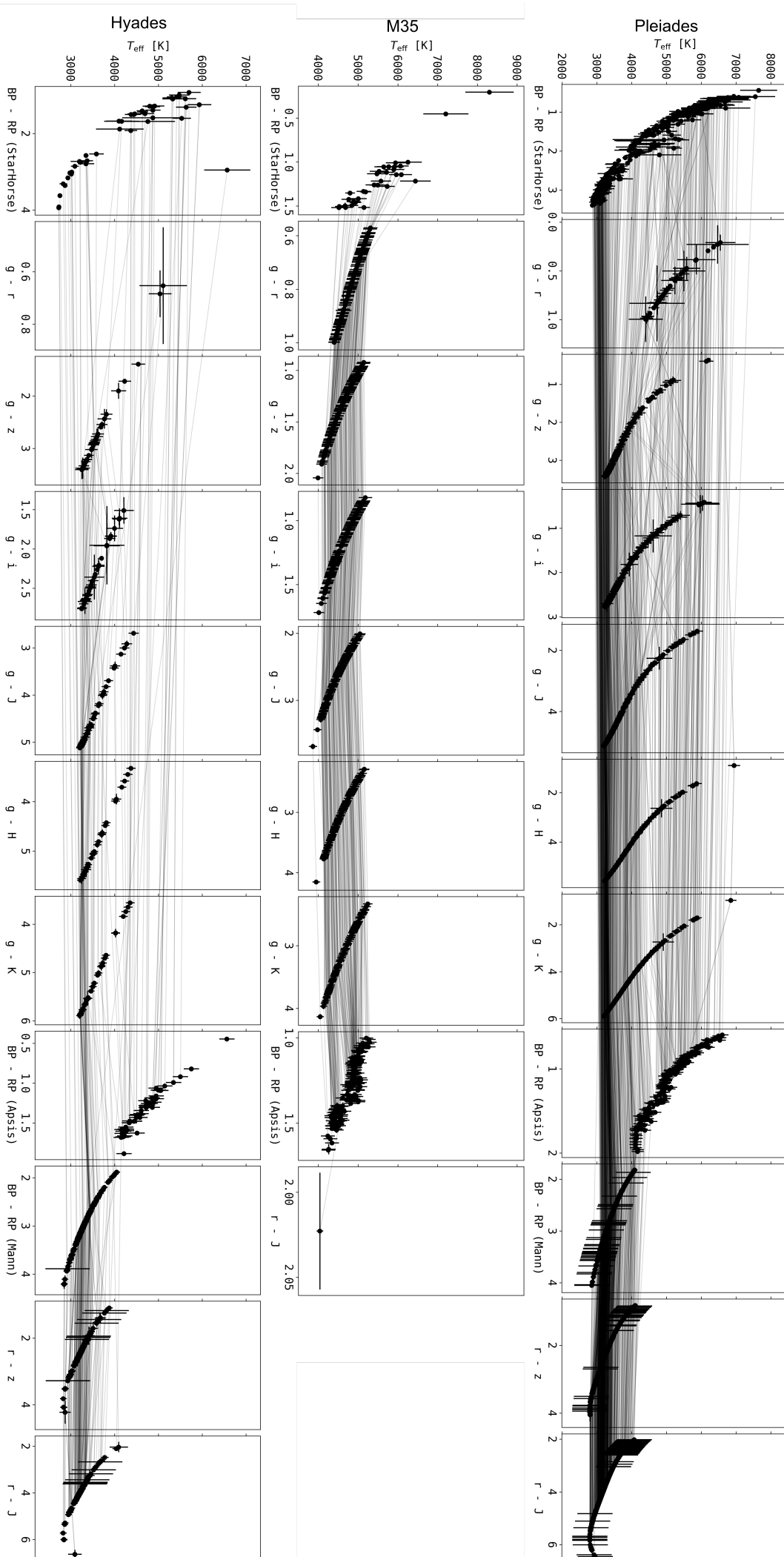


Table 1. Open clusters.

cluster	<i>n</i>	LCs	SLCs	LLCs	PSF LCs	age[Myr]	distance[pc]	[Fe/H]
Pleiades	2033	944	33	911	0	125		
M35	1614	5	0	5	158			
Hyades	655	301	42	259	0			
Praesepe	1281	2500	68	2432	0			
Rup 147	213	97	25	72	0			
M67	1344	1141	118	1023	1019			

Notes. *n* is the approximate number of members with $p > 0.8$. LCs, SLCs, LLCs, and PSF LCs denote the number of available light curves, short cadence light curves, long cadence light curves, and PSF de-detrended light curves, respectively. The values for age, [Fe/H], and distance are approximate values from a comparison of existing literature, detailed in Appendix B.1.

113 2.4. Effective temperatures, stellar radii, and luminosities 160

114 We determined effective temperatures T_{eff} using broadband 161
 115 photometry from the Tycho catalog, UCAC4, the Two Micron 162
 116 All Sky Survey (2MASS; Skrutskie et al. 2006), the Panoramic 163
 117 Survey Telescope and Rapid Response System (Pan-STARRS) 164
 118 Data Release 1 (Chambers et al. 2016), and Gaia DR2 (Gaia 165
 119 Collaboration et al. 2018b). We applied different quality cuts, 166
 120 2MASS, Pan-STARRS DR1, and GaiaDR2 data, as described 167
 121 in Appendix C, and removed foreground stars using Gaia DR2 168
 122 parallaxes. 169

123 Using a catalog of touchstone stars, compiled and complemented 170
 124 by Yee et al. (2017) and the T-R relations in Mann et al. 2015 171
 125 we assigned stellar radii R_* and empirical spectra according 172
 126 to the targets' T_{eff} and [Fe/H]. We then combined stellar radii 173
 127 R_* , T_{eff} , and spectra to projected bolometric luminosities L_{bol} ,¹⁷⁴
 128 and projected luminosities in the Kepler band $L_{\text{Kp},*}$ (Shibayama 175
 129 et al. 2013; Ilin et al. 2019). 176

130 Color-temperature relations (CTRs) from Boyajian et al. (2013)¹⁷⁷
 131 and Mann et al. (2016) (erratum to Mann et al. 2015) yielded 178
 132 T_{eff} .¹⁷⁹

133 Boyajian et al. (2013) determined CTRs from a range¹⁸⁰
 134 interferometrically characterized stars using $g - z$, $g - i$, $g - z$ ¹⁸¹
 135 $g - J$, $g - H$, and $g - K$ colors from SDSS and Johnson¹⁸²
 136 magnitudes for A to K stars. Their sample is centered on solar¹⁸³
 137 metallicity, so we constrained the use of these CTRs to stars with¹⁸⁴
 138 $-0.25 < [\text{Fe}/\text{H}] < 0.25$. We transformed 2MASS JHK to $J - H$ ¹⁸⁵
 139 $H - K$, and $J - K$ in the Johnson system as the authors from¹⁸⁶
 140 2MASS to the Bessell-Brett system (Carpenter 2001), and from¹⁸⁷
 141 Bessell-Brett to Johnson using the relations in Bessell & Brett¹⁸⁸
 142 (1988). We corrected the 2MASS and PanSTARRS photometry¹⁸⁹
 143 in M35, M67, and Ruprecht 147 for extinction using the most¹⁹⁰
 144 recent version (Green et al. 2019) of the dustmaps package that¹⁹¹
 145 provides 3D dust maps derived from 2MASS and PanSTARRS¹⁹²
 146 photometry together with Gaia distances (Green et al. 2018).¹⁹³
 147 If an extinction value was not available for a given star¹⁹⁴
 148 used the average extinction value of the respective cluster. We¹⁹⁵
 149 accounted for extinction in Gaia BP and RP using the reddening¹⁹⁶
 150 $E(\text{BP}-\text{RP})$ derived from Gaia photometry and parallax from¹⁹⁷
 151 Gaia DR2 (Andrae et al. 2018).¹⁹⁸

152 Mann et al. (2015) provide CTRs from absolutely calibrated¹⁹⁹
 153 spectra to which they fitted atmospheric models to obtain T_{eff} .²⁰⁰
 154 Alternatively, they determined T_{eff} from long-baseline optical²⁰¹
 155 interferometry measurements using the bolometric flux. Among²⁰²
 156 others, they note transformations for SDSS/2MASS $r - z$ and²⁰³
 157 $r - J$, or Gaia $BP - RP$ where extra information can be added²⁰⁴
 158 from metallicity or 2MASS $J - H$. The relations in Mann et al.²⁰⁵
 159 (2015) are only valid if metallicity is sufficiently close to solar.²⁰⁶

which is satisfied for all clusters in this paper (see Table ??).
 M35 may be an exception to this rule.

StarHorse

Gaia DR2 published effective temperatures for over 160 million sources (Gaia Collaboration et al. 2018b). The typical uncertainty is quoted at 324 K, but it is lower for stars above ~ 4000 K and below ~ 6700 K, so that we adopt 175 K which is above the quoted root-median-squared error in this T_{eff} range (Andrae et al. 2018).

Empirical CTRs suffer from systematic errors that stem both from the different methods applied, and from sample selection biases. We used as many empirical relations as possible in their appropriate ranges to obtain multiple T_{eff} estimates from which we then drew a more reliable median value. Targets that were lacking sufficient photometric data to derive T_{eff} , or were too hot to be expected to have a convective envelope, were flagged accordingly, and removed from the sample. These excluded data can be retrieved from the online material.

We used a catalog of empirically characterised stars (Yee et al. 2017) to derive R_* . Yee et al. (2017) collected 404 stars with high-resolution spectra from the literature, and own observations of mid to late K-dwarfs, spanning low mass stars from 7000 K down to 3000 K. For these stars, the resulting catalog is accurate to 100 K in T_{eff} , 15 % in R_* , and 0.09 dex in [Fe/H]. We matched stars from the catalog to our derived Teff within uncertainties and propagated the resulting scatter to the uncertainty in R if Teff > 3500 K. For stars with Teff < 3500 K we used Mann et al. T-R relations.

3. Methods

We detected and validated flare candidates automatically. We assigned recovery probabilities and corrected for sampling effects using injection/recovery tests for different flare morphologies. Most of the candidates are expected to have a complex shape that deviates from the classical flare template. The validation yielded an estimate on the uncertainty on the flare energy released in the Kepler band. The frequency distributions of these flare energies are believed to follow a power law that spans multiple orders of magnitude. We adopted this model, and used two different Maximum Likelihood estimators to obtain the power law exponents. We tested the best fit parameters with the Kolmogorov-Smirnov test, and probed possible truncation of the power law relation with an exceedance test.

¹ <https://k2.hatsurveys.org/archive/>

203 **3.1. Flare finding**228 **3.3. Complex Flares**

We used the open source software AltaiPony² to automatically detect and characterize flares in our sample. The code base lies on K2SC³ (Aigrain et al. 2016) to remove instrumental astrophysical variability from K2 light curves. We did not use pre-detrended light curves available on MAST, but used K2SC to derive our own, because we clipped outliers at 3σ , as compared to the original work, where outliers were clipped at 5σ (Aigrain et al. 2016).

After de-trending, the flare finder algorithm looked for continuous observing periods, defined as being longer than 10 points at a minimum cadence of 2 h. All further routines were run on these observing periods. The finder iteratively clipped excursions from the median value at 3σ rolling window above median plus uncertainty given from K2SC de-trending. After each iteration, outliers were cut down to the current median value. Either after convergence, or 50 iterations, the resulting median value was adopted. With this median, flare candidates were identified with the same procedure as during the median value calculation, but now we additionally required at least three consecutive data points to fulfil the σ -criterion. Flare candidates were merged into single candidate events if they were no more than three data points apart. For each of these candidates, the amplitude and equivalent duration (ED) was returned.

The Kepler flare sample has shown to be difficult to treat in a fully automated way. Without manual vetting, the event samples remain significantly contaminated (Yang & Liu 2019). We reduce the number of potential false positives using SkyBoT. ED is the area between the LC and the quiescent flux, that is, the integrated flare flux divided by the median quiescent flux of the star, integrated over the flare duration (Hunt-Walker et al. 2012):

$$ED = \int dt \frac{F_{flare}(t)}{F_0}.$$

ED is a quantity independent of calibration and distance that is suited to compare flaring activity on stars where these properties are uncertain. It describes the time during which a star releases much energy as the flare itself. This time can be short or longer than the actual flare duration.

209 **3.2. Recovery probability and ED correction**267 **3.5. Power law fits**

To further validate the flare events, every candidate was injected to its light curve of origin several times with varying amplitude and duration using a classical flare template (Davenport et al. 2014). This returned a recovery probability of similar morphologies on a given light curve. We accepted a candidate if the recovery probability was above 80 %. From the difference between injected and recovered values we calculated individual correction factors for all candidates that typically increased the ED because the 30 min time sampling systematically underestimates the ED (Yang et al. 2018) as compared to short cadence observations. Corrected flare EDs from injection-recovery validated candidates were then converted to $E_{Kp,flare}$ and passed to further analysis.

How is recovery affected by GP Regression?

Can we isolate sampling effects?

Can we do a simpler correction by showing that most of the ED under-estimate comes from the under-sampling at 30 min cadence?

Complex flares are flaring events that do not follow the classical time evolution (Davenport et al. 2014). In many cases, observed flares can be described by superimposing multiple single events. We call these flares complex. Some flares cannot be described in this way. We call these flares atypical. Davenport et al. (2014) found 60 – 80 % of flares with duration of more 50 min to have multiple peaks, and successfully fitted them a superposition of multiple classical events to them on active M dwarf GJ 1243. However, 1.3 % of all flare detections were atypical. In the long cadence data present here, flare durations were at least 1.5 h, and thus likely most of our candidates have a complex morphology. The time resolution, however, bars us from reconstructing the individual morphologies directly... *How complex was complex (2 flares overlap, or rather 10? Does this depend on energy?*

3.4. Kepler flare energies

(see PaperI for details).

Multiband time resolved observations of active M dwarfs have shown that continuum flux accounts for the majority of the energy radiated by flares (Kowalski et al. 2013). The effective temperature of this blackbody, however, varies by a great degree, with, to date, no robust predictor of that temperature:

While solar flares are relatively cool, with $T_{eff} \approx 5\,000 - 7\,000$ K (Kleint et al. 2016; Kerr & Fletcher 2014; Watanabe et al. 2013; Namekata et al. 2017), at least one M dwarf flare reached 40 000 K as seen in FUV spectra (Froning et al. 2019), and most events exhibit temperatures of about 9 000 – 10 000 K (Hawley & Fisher 1992; Kretzschmar 2011; Shibayama et al. 2013). A dependence of flare temperature on stellar age, or mass, or both, will enter our analysis if we attempt to quantify bolometric flare energy. At about 6 200 K, the Kepler pass band captures the largest flux fraction, at 10 000 K 72 %, at 40 000 K only 4% of this value is transmitted. Another effect is that flares of equal flare energy but hotter SED would not be seen in the Kepler band at all.

We propagated the uncertainties σ_{ED} and σ_L (on $L_{*,Kp}$) in quadrature to $E_{Kp,flare}$.

We derived σ_{ED} empirically from the injection and recovery of synthetic flares. It is determined from the standard deviation in correction factors f_{ir} between injected and recovered ED . f_{ir} is a function of flare amplitude and duration. Uncertainties on amplitude and duration are also derived empirically from injection and recovery of synthetic flares.

We propagated the uncertainties on σ_L from uncertainties on photometry, extinction correction, and empirical color– T_{eff} relations (Mann et al. 2016) for which the photometry was used. Uncertainties on the stellar radius were obtained from $T_{eff} - R_*$ relations (Mann et al. 2016). Both, color– T_{eff} and $T_{eff} - R_*$ relations, included the uncertainties on [Fe/H] that we collected from the literature.

3.5. Power law fits

Flare frequency distributions follow power law relations that cover several orders of magnitude, from solar microflares to stellar superflares. We fitted power law functions to the FFDs using three different approaches.

The first method was a maximum likelihood estimator (MLE) from Maschberger & Kroupa (2009).

The second method used the MLE result as a prior for α . Following Wheatland (2004), we defined the joint posterior distribution

² <https://github.com/ekaterinailin/AltaiPony>

³ <https://github.com/OxES/k2sc>

287 for the probability ϵ that a flare with ED or energy above some
 288 value S_2 occurs within a time period ΔT :

$$\begin{aligned} p(\epsilon, \alpha) &= C \cdot (-\ln(1 - \epsilon))^M \\ &\cdot (\alpha - 1)^M \cdot \Gamma(\alpha) \left[\frac{(S_2/S_1)^{M+1}}{\pi} \right]^\alpha \\ &\cdot (1 - \epsilon)^{(T/\Delta T) \cdot (S_2/S_1)^{\alpha-1} - 1}. \end{aligned} \quad (2)$$

289 C is the normalisation constant, M is the number of events,
 290 the total observation time. Γ contains the prior distribution for α ,
 291 and S_1 denotes the detection threshold above which all flares are
 292 detected. π encapsulates the flare energies as

$$\pi = \prod_{i=1}^M \frac{s_i}{S_1}$$

293 , where $\{s_1, s_2, \dots, s_m\}$ are the flare energies or ED .
 294 The posterior distribution in Wheatland (2004) captures both
 295 Poissonian distribution of flare events in time, and their power
 296 law distribution in energy, simultaneously. Wheatland (2004)
 297 derived this model to be able to predict the flaring rate of a
 298 given active region on the sun, and offered an extension to Eq.
 299 2 that treated changing flaring activity rates as the active region
 300 evolves, and also characteristics of the active region itself, such
 301 as sunspot classifiers. In our simplification of the model, we
 302 assumed that the flare generating process did not change within
 303 the observation time span in any star in our sample ($M = M'$ in
 304 Eq. 24 in Wheatland (2004)). Another assumption was that this
 305 process was the same for all stars in the sample ($\Lambda_{MC} = 1$ in Eq.
 306 24). Thus the information gained from the light curves could be
 307 stacked together.

308 While in the case of a uniform prior for α the results from the MLE and Markov Chain Monte Carlo (MCMC)
 309 sampling from the posterior distribution are the same, the latter allowed us to fit for ϵ and α simultaneously. Additionally, the MCMC approach can be extended to incorporate further information about the stars in the sample in the future.

310 Another advantage of the latter approach is that we could use more informative priors. We also used a Gaussian fit to α obtained from the posterior distribution using the full sample flares as the prior for a subsequent Bayesian analysis of individual age and T_{eff} bins. Assuming that α is universal for all spectral types, ages, and flare energy ranges, we used this more informative, Gaussian prior to further constrain the flaring rates.

311 The uncertainties on α were computed using the jackknife algorithm, which is well suited if we suspect false positives among the flare candidates. The resulting uncertainty estimate reflects the weight of outliers in the data. To show this, we sampled 100 random FFDs of the same size, best fit power law parameters, and minimum and maximum observed ED for each power law fit we performed. We compared the power law parameters derived for these FFDs with the above methods to the original value, and found that the jackknife uncertainty captures XX% of random FFDs' results. With all methods, we fitted the intercept β_{cum} using non-linear least squares to the cumulative FFD and converted the result to $\beta = \beta_{\text{cum}} \cdot |\alpha - 1|$. As with α , we calculated the uncertainty $\sigma_{\beta_{\text{cum}}}$ using the jackknife algorithm, and propagated uncertainties from α for the final result on β .

312 Additionally we calculated the exceedance statistic tr to test if the power law distribution was truncated. If tr is 1, the power law distribution is truncated at the high energy end. If tr is 0, no information was gained from the calculation. To derive tr , given a number n of observations X_n and a best fit value for the power law exponent, we generated 500 samples with n values

313 from this best-fit distribution assuming no truncation, i.e. choosing an upper limit several orders of magnitude higher than X_{max} .
 314 We then proceeded to truncate the samples at thresholds T below the maximum observed value X_{max} and determined the average number N_{ex} of generated values that will exceed T . If the underlying power law is not truncated, N_{ex} declines with larger n , as larger X_{max} will be present in the original data. If the best fit power law exponent is steeper, N_{ex} will be underestimated. If the best fit power law exponent is flatter, N_{ex} will be overestimated. If the power law is not truncated, for $n \geq 100$ N_{ex}/n will be $< 5\%$, for $20 < n < 100$, typically $N_{\text{ex}}/n < 15\%$.

315 As recommended by Maschberger & Kroupa (2009), we applied the stabilized Kolmogorov-Smirnov (KS) test at 95 % significance level to all power law fits in the sample. If the test fails the power law model does not fit the data at the given significance level. If the test passes, this does not give any information whether the power law model is the correct assumption. The goodness of fit can be estimated from the visual inspection of percentile-percentile plots, given in the online material⁴.

4. Results

361 Fig. 4 shows the $E_{Kp, \text{flare}}$ and ED detection thresholds, as defined
 362 by the recovery probability (see Sec. 3.2). The thresholds in ED
 363 reflect the noise level in the light curves.

4.1. Flaring activity as a function of age and T_{eff}

364 Flaring activity decays with age. Flaring fraction was observed to decline with galactic latitude for M dwarfs (Hilton et al. 2010) Howard+2019. Short rotation periods and high magnetic activity measured in $H\alpha$ are strongly correlated (West et al. 2015). According to gyrochronology, fast rotation indicates young age (Barnes 2003), and slows down as the star ages. Here, we quantify how this decline unfolds for different spectral types. Except for the stars in our coolest temperature bin (M5.5-M8, 2 500-3 000 K), stellar flaring activity at a given age is always stronger for a cooler star. The exception is seen at cluster ages around 120 Myr.

4.2. M67

365 We found one very likely flare candidate in the PSF-detrended light curves (Nardiello et al. 2016). After having searched the entire sample we identified about 250 candidates. We excluded those candidates that clustered spatio-temporally in different light curves as systematics. After vetting the remaining 25 by eye, we excluded false positives judging by their morphology, leaving a mere ten light curves with flare-like shape. One target appeared to be an echo from one of the other light curves. Five targets were foreground stars, two are more likely background stars, one target is probably a giant and does not appear in Gaia photometry (IR source). Only one target appears to reside at M67 distance and is a $p = 0.997$ member according to Gao (2018). The 2MASS and Gaia BP and RP colors indicate an M2V dwarf (Pecaut & Mamajek 2013). If the spectral class is correct, the flare releases about $6.1 \cdot 10^{33}$ erg ($ED = 1391 \pm 548$ s) in the Kepler band.

⁴ [https://github.com/ekaterinailin/](https://github.com/ekaterinailin/flares-in-clusters-with-k2-ii)
 flares-in-clusters-with-k2-ii

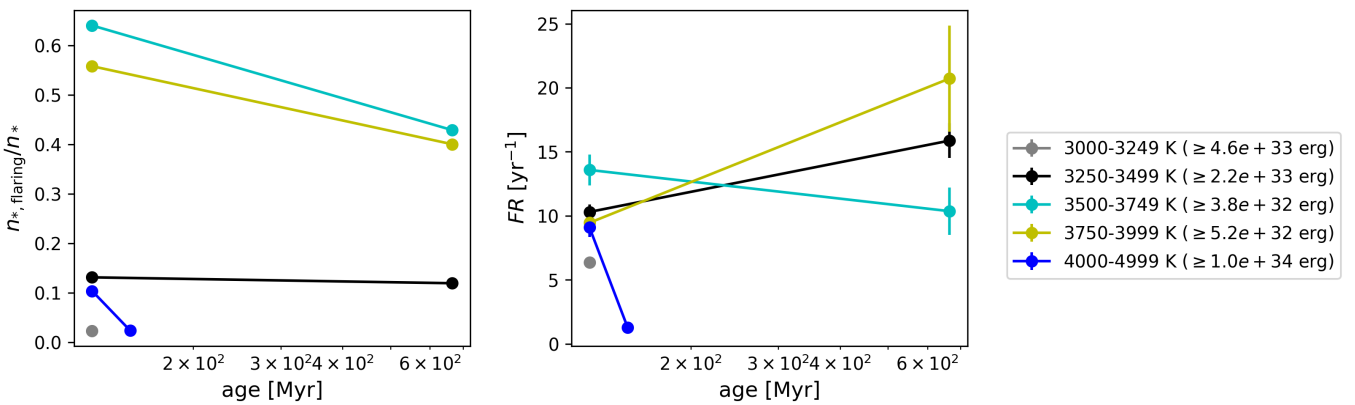


Fig. 3. Flaring activity in energy distributions. Left panel: Flaring fraction $n_{\star, \text{flaring}}/n_{\star}$. Right panel: Flaring rate FR . See Fig. 4 for details on the overall figure layout.

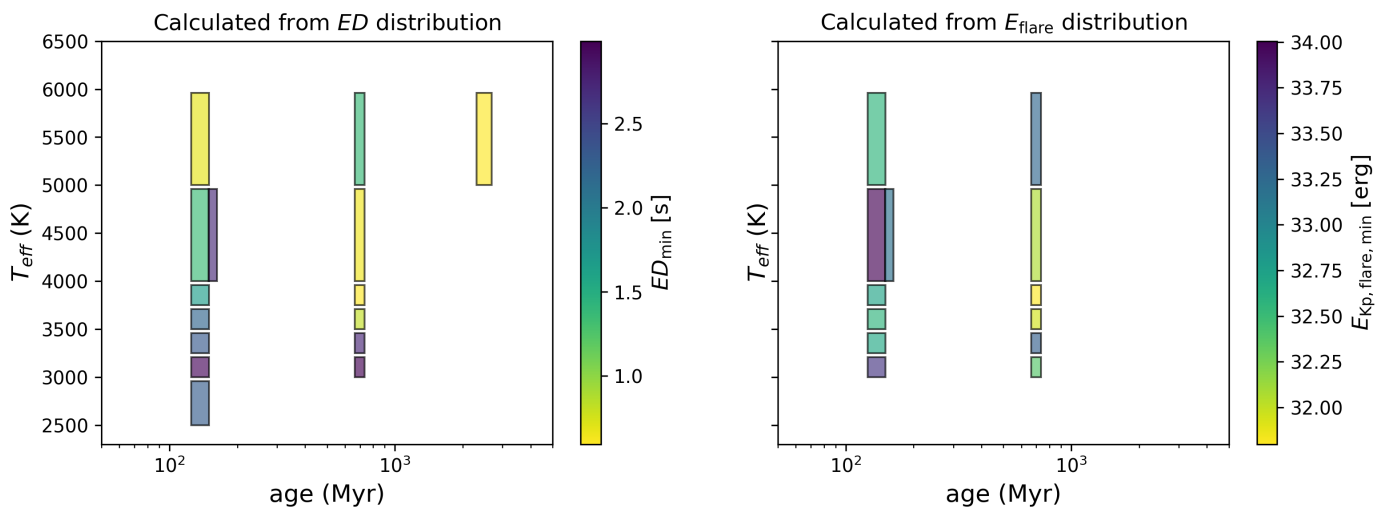


Fig. 4. E_{flare} and ED detection thresholds as a function of stellar age and T_{eff} . The rectangles' widths on the age axis reflect the uncertainty on the cluster ages found in the literature. The rectangles' widths on the T_{eff} axis encompass the temperature bins over which the thresholds were averaged.

393 4.3. Flaring Activity Indicators

394 Flaring rates: FR and flaring fraction We define FR as the flare
 395 rate above detection thresholds on $E_{\text{Kp,flare}}$ and ED in each T_{eff}
 396 bin, respectively (Figs. 5 and 6).

Flaring energy: FA and $L_{\text{Kp,flare}}$ The energy released in flares was inferred using our derived stellar luminosities. It declines with age for every T_{eff} bin considered for both the total luminosity and relative to the quiescent flux (Fig. 7).

$L_{\text{Kp,flare}}$ is the luminosity in flares in the Kepler band. We can relate this to the quiescent bolometric luminosity of the star where we define the fractional flare luminosity FA as in PaperI:

$$FA = \frac{1}{N} \sum_i^N FA_i = \frac{1}{N} \sum_i^N \frac{E_{\text{Kp,flare,tot},i}}{t_i \cdot L_{\text{bol},*,i}}$$

We determine $L_{\text{bol},*}$ from R_* and T_{eff} , as described in Sec. 2.4. This is a meaningful measure of relative stellar activity as long as only the flux portion of the quiescent star in the Kepler band is roughly constant. It is therefore sensible to compare FA values across ages, but not across T_{eff} .

402 FFD Power law fit parameters to the FFDs (Figs. 8 and 9) are
 403 sensitive to the low-energy cutoff, where most observations reside. The goodness of fit strongly depends on the sample size.
 404 Power law fit parameters derived using MLEs, as described in
 405 Sec. 3.5, are mostly consistent with each other but often deviate
 406 from $\alpha = 2$. A smaller sample size tends to create a flatter distribution (Figs. 10 and 11). Truncation was not detected for FFDs
 407 with more than 50 flares (Tables 2 and 3) For these results, ex-
 408 trapolations outside of the observed energy range are clearly off.
 409 If we assume $\alpha \equiv 2$, different distributions can be compared. For
 410 fixed α , in the ED domain, β_2 is the flare frequency at $ED = 1$ s,
 411 and shows a trend in both T_{eff} , and age (see Fig. 13). In the en-
 412 ergy domain, the picture is less clear (Fig. 12).

413 Compare to other FFD values, e.g., from Ward's Evryscope sur-
 414 vey, see table in Appendix, and maybe convert it to a plot Howard
 415 et al (2019) monitored superflares on cool stars with bolometric
 416 energies above 10^{33} erg and up to 10^{36} erg. They find power law
 417 exponent values around ~ 2 resolved by spectral types. Similar
 418 values are found for individual flare stars (Lurie et al. 2015).
 419 Howard+18, Loyd+18, Tilley+19 show that flares can erode ex-
 420 planetary atmospheres. If a flare is assumed to deposit its UV
 421 energy in an instant a single superflare can completely remove
 422 423

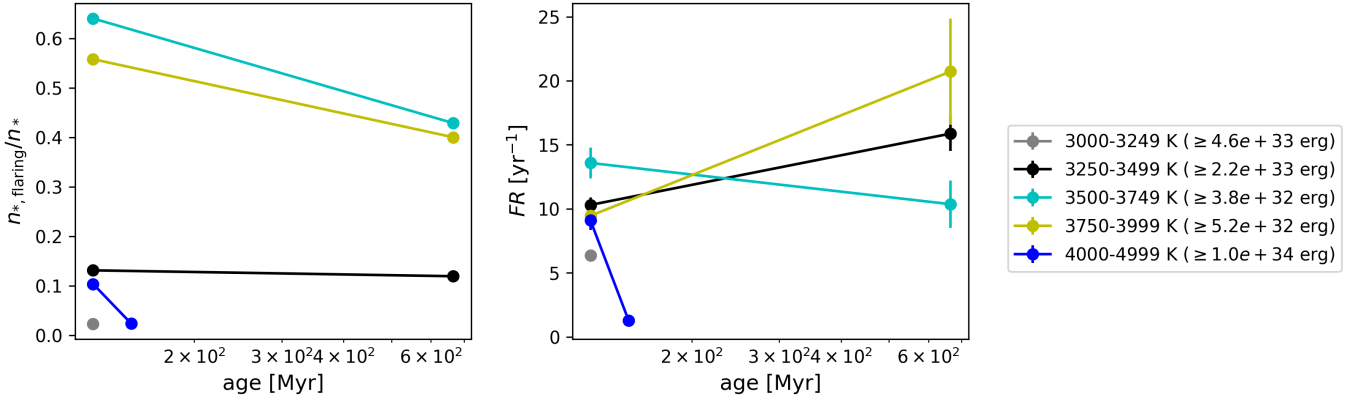


Fig. 5. Flaring activity in energy distributions. Left panel: Flaring fraction n_{flaring}/n_* . Right panel: Flaring rate FR . See Fig. 4 for details on the overall figure layout.

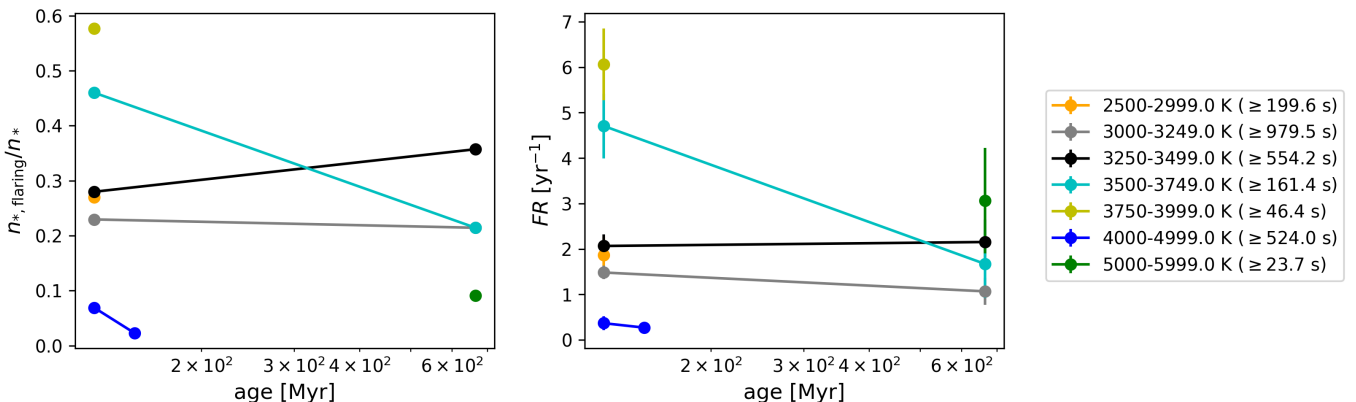


Fig. 6. Flaring activity in ED distributions. Left panel: Flaring fraction n_{flaring}/n_* . Right panel: Flaring rate FR . See Fig. ?? for details on the overall figure layout.

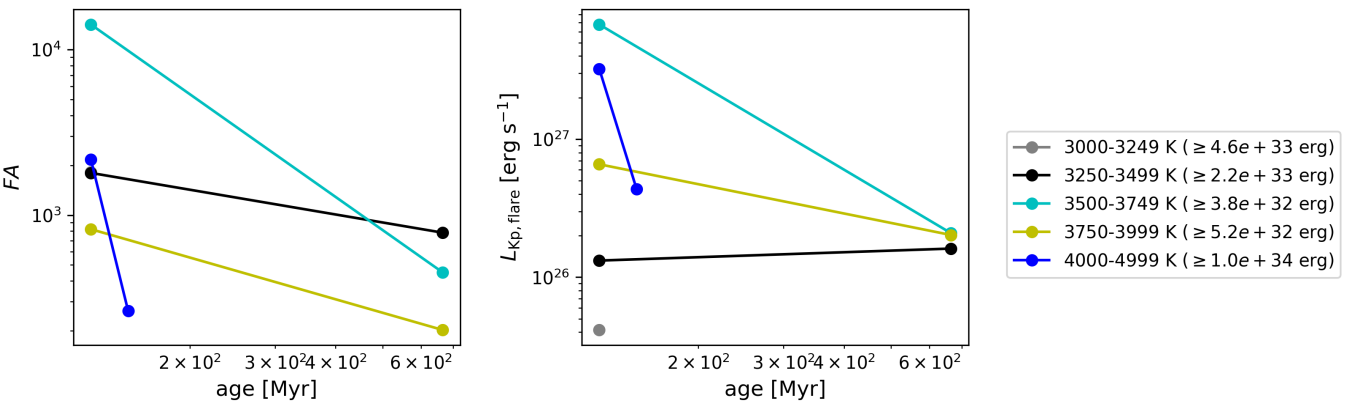


Fig. 7. Energy released in flares. Left panel: Energy released in flares relative to quiescent stellar luminosity FA . Right panel: Average flaring luminosity released in the Kepler band $L_{Kp,\text{flare}}$.

424 the ozone layer at the substellar point Loyd+18. Associated p₄₂₇
425 tons are safer way to ozone destruction if they are associated
426 with reoccurring large flares Tilley+19

5. Discussion

5.1. Flaring and rotation

429 More energetic flares can be expected from faster rotating
430 stars (Candelaresi et al. 2014; Doorslaere et al. 2017; Yang
431 et al. 2017). Findings that flares with intermediate Rossby num-
432 ber appear to flare more than fast and slow rotators (Mondrik

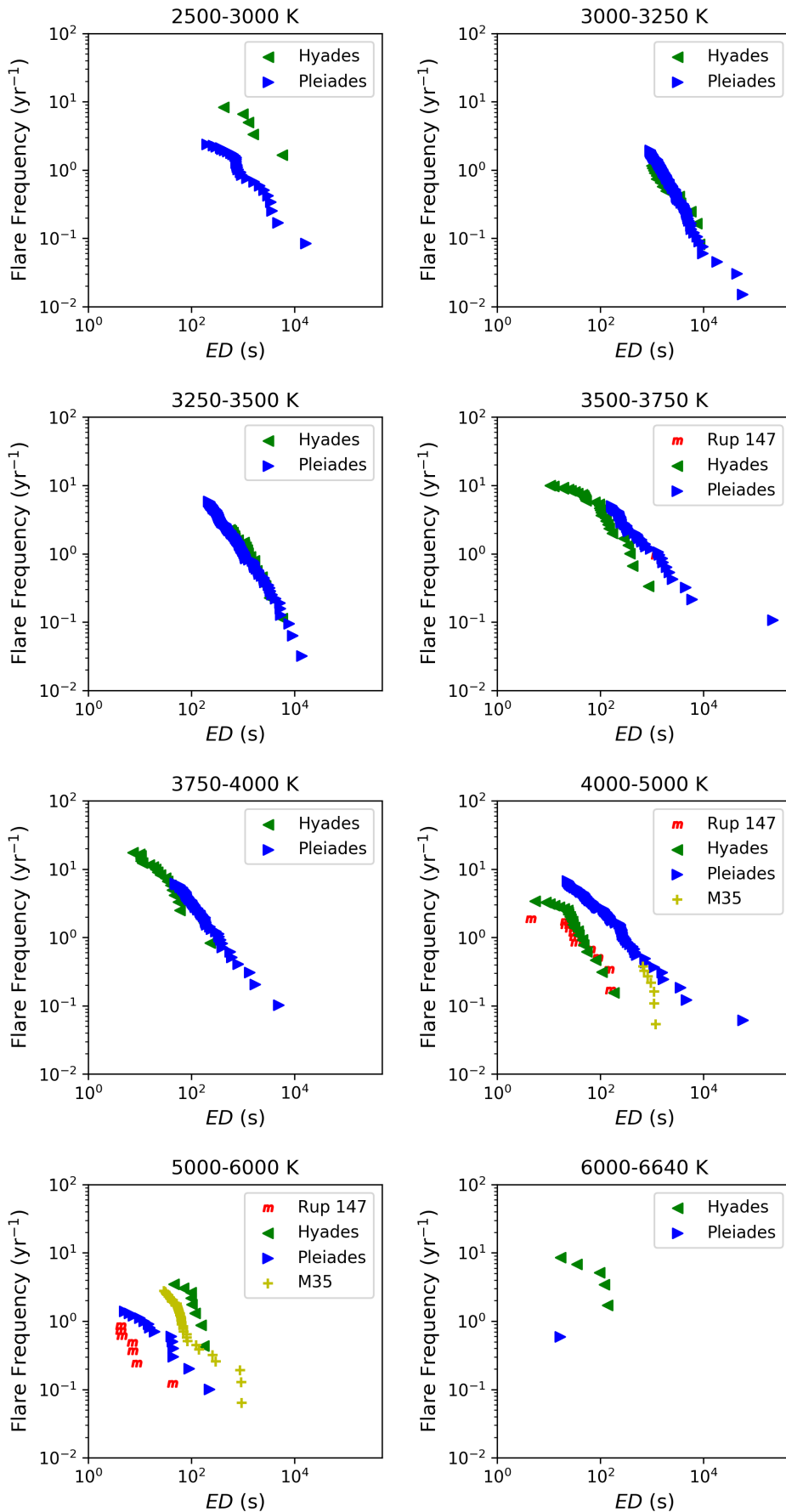


Fig. 8. Cumulative flare frequency distributions (FFDs) of equivalent durations (ED). In each panel, every distribution belongs to one cluster. The panels are binned by T_{eff} .

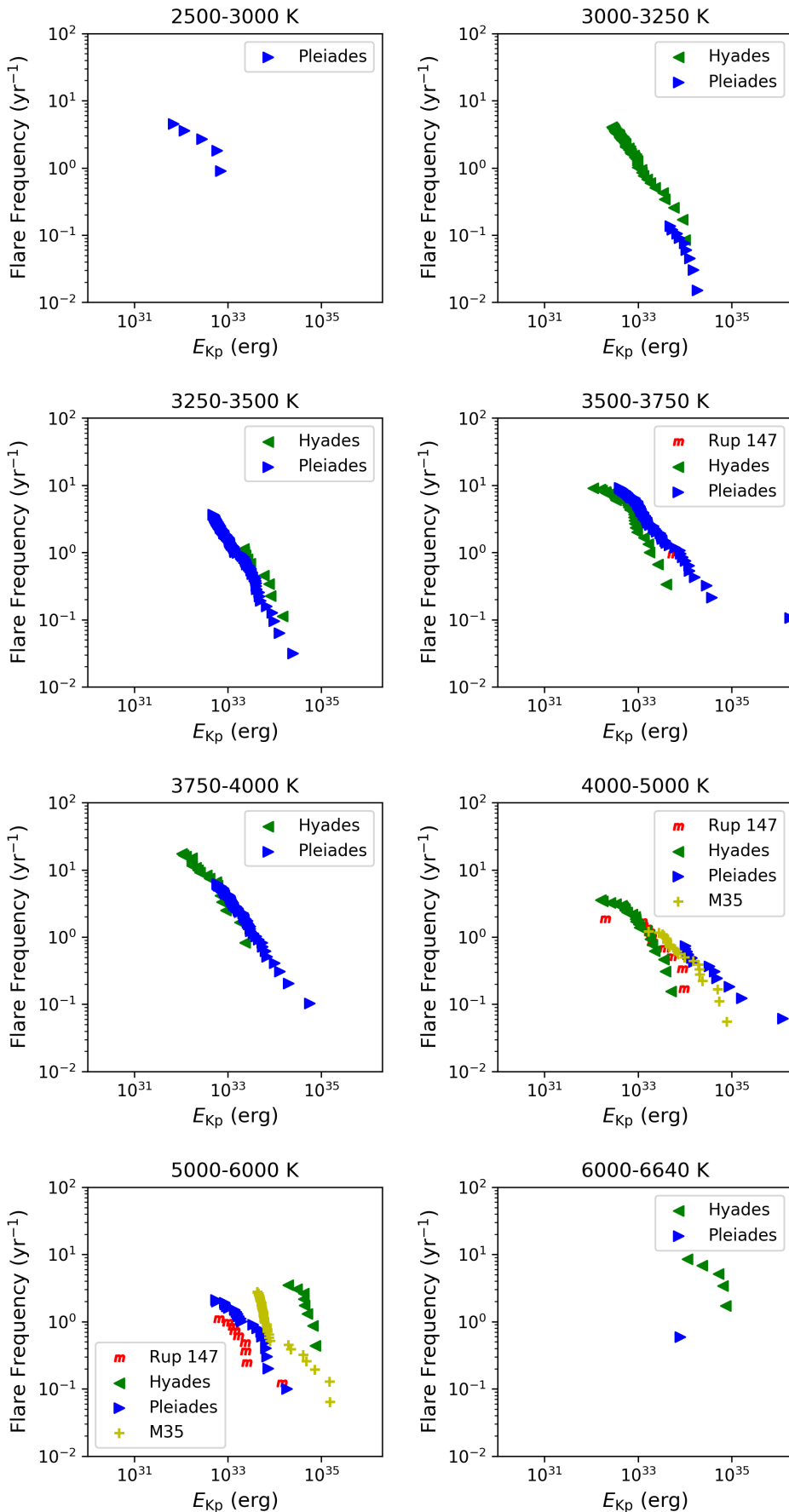


Fig. 9. Same as Fig. 8, but of Kepler flare energies $E_{\text{Kp,flare}}$.

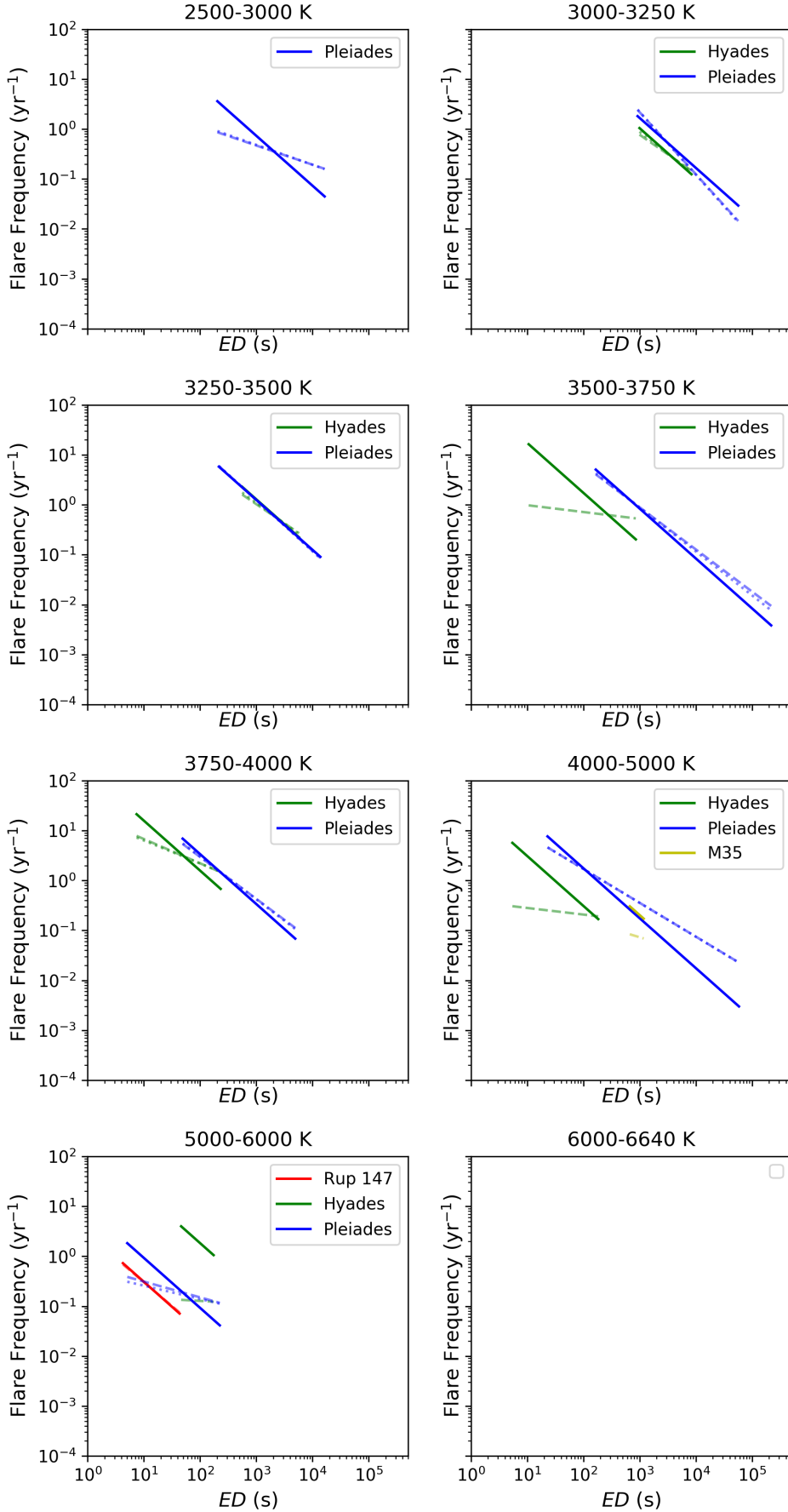


Fig. 10. Power law fits to the FFDs of ED in Fig. 8. Bold line: a power law with $\alpha = 2$. Dashed line: best fit parameters were determined following Maschberger & Kroupa (2009) (see Sec. XX). Dotted line: best fit parameters were determined following Bauke (2007) (see Sec. XX)

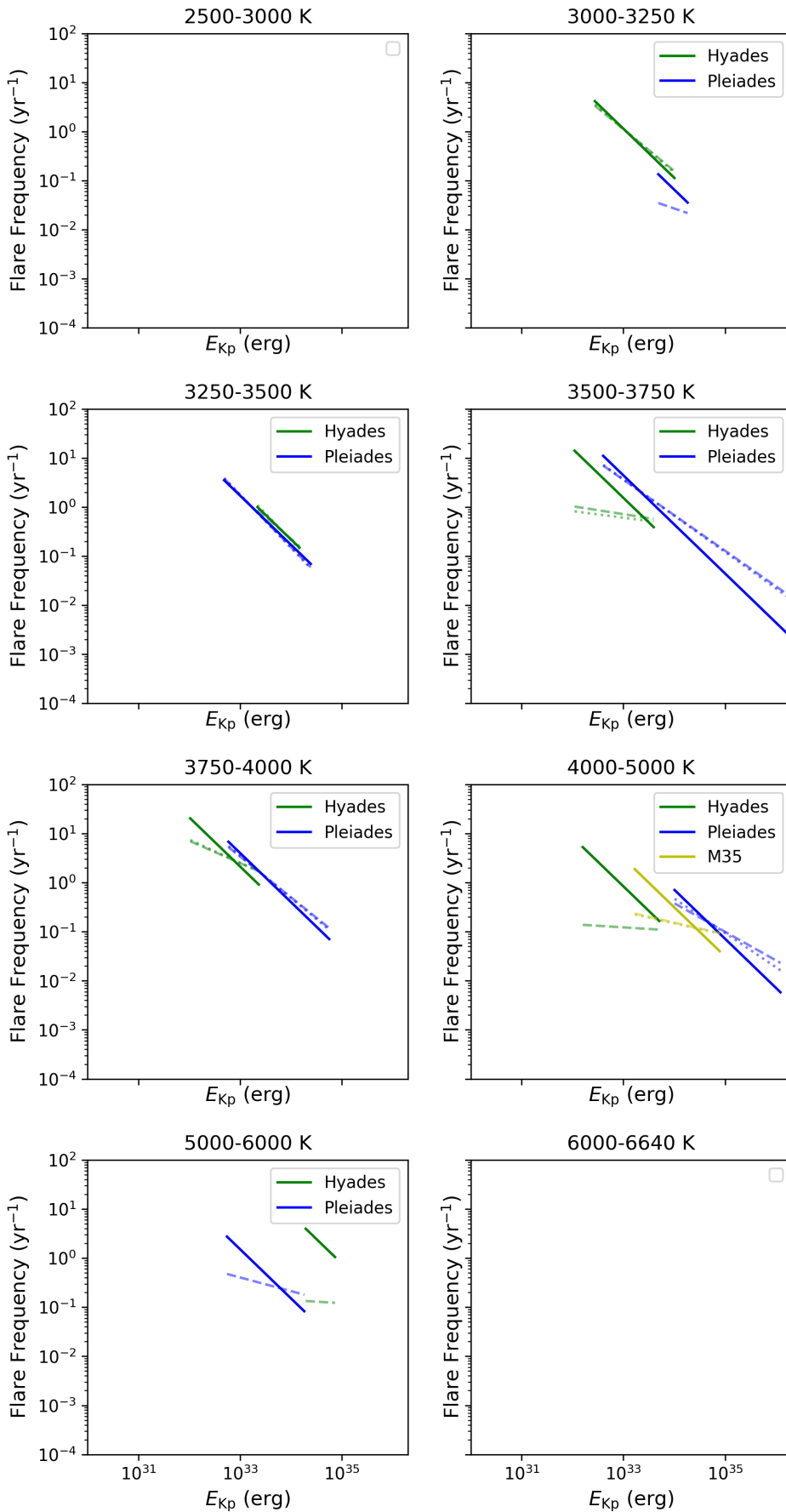


Fig. 11. Power law fits to the FFDs of $E_{Kp,\text{flare}}$ in Fig. 8. See Fig. 10 for details.

Table 2. Summary of activity parameters of all clusters and T_{eff} bins in energy distributions.

cluster	$T_{\text{min}} [\text{K}]$	$T_{\text{max}} [\text{K}]$	n_s	n_{flares}	age [Myr]	[Fe/H]	$E_{\text{Kp,flare,min}} [\text{erg}]$	α_{B}	β_2 [yr^{-1}]	β_{MK} [yr^{-1}]	tr_{B}	tr_{MK}
Pleiades	4000	4999	87	148	125 ± 25	-0.02 ± 0.03	$1 \cdot 10^{34}$	1.70 ± 0.24	1.58 ± 0.20	$7.19 \cdot 10^{33} \pm 2.32 \cdot 10^{32}$	$2.07 \cdot 10^{23} \pm 5.12 \cdot 10^{32}$	$1.39 \cdot 10^{19} \pm 2.87 \cdot 10^{18}$
Pleiades	3000	3249	353	420	125 ± 25	-0.02 ± 0.03	$4.6 \cdot 10^{33}$	1.35 ± 0.42	$6.57 \cdot 10^{32} \pm 1.60 \cdot 10^{31}$	-	$1.09 \cdot 10^{10} \pm 4.74 \cdot 10^9$	0
Pleiades	3250	3499	168	324	125 ± 25	-0.02 ± 0.03	$4.8 \cdot 10^{32}$	2.08 ± 0.12	2.06 ± 0.11	$1.71 \cdot 10^{33} \pm 6.95 \cdot 10^{30}$	$1.97 \cdot 10^{35} \pm 9.34 \cdot 10^{34}$	0
Pleiades	3750	3999	92	125	± 25	-0.02 ± 0.03	$5.2 \cdot 10^{32}$	1.86 ± 0.12	1.83 ± 0.11	$4.01 \cdot 10^{33} \pm 4.99 \cdot 10^{31}$	$7.09 \cdot 10^{28} \pm 8.49 \cdot 10^{27}$	0
Pleiades	5000	5999	53	23	125 ± 25	-0.02 ± 0.03	$3.7 \cdot 10^{32}$	-	$1.51 \cdot 10^{33} \pm 1.56 \cdot 10^{32}$	-	$1.66 \cdot 10^{8} \pm 5.19 \cdot 10^7$	0
Pleiades	3500	3749	50	127	125 ± 25	-0.02 ± 0.03	$3.8 \cdot 10^{32}$	1.74 ± 0.09	1.72 ± 0.09	$4.44 \cdot 10^{33} \pm 8.32 \cdot 10^{31}$	$7.47 \cdot 10^{24} \pm 6.80 \cdot 10^{23}$	$1.93 \cdot 10^{24} \pm 1.70 \cdot 10^{23}$
M35	4000	4999	216	23	149 ± 13	-0.21 ± 0.06	$1.6 \cdot 10^{33}$	1.23 ± 0.32	1.24 ± 0.27	$3.15 \cdot 10^{33} \pm 5.31 \cdot 10^{32}$	$2.20 \cdot 10^{6} \pm 7.14 \cdot 10^5$	$4.81 \cdot 10^6 \pm 1.34 \cdot 10^6$
Hyades	4000	4999	32	24	665 ± 70	0.13 ± 0.01	$1.2 \cdot 10^{32}$	-	1.06 ± 0.14	$8.40 \cdot 10^{32} \pm 1.54 \cdot 10^{32}$	-	$1.07 \cdot 10^9 \pm 1.83 \cdot 10^{-1}$
Hyades	3000	3249	54	115	665 ± 70	0.13 ± 0.01	$2.5 \cdot 10^{32}$	1.89 ± 0.18	1.85 ± 0.17	$1.15 \cdot 10^{33} \pm 6.45 \cdot 10^{30}$	$1.93 \cdot 10^{29} \pm 3.51 \cdot 10^{28}$	$1.33 \cdot 10^{28} \pm 2.28 \cdot 10^{27}$
Hyades	3250	3499	42	140	665 ± 70	0.13 ± 0.01	$2.2 \cdot 10^{33}$	2.09 ± 0.65	1.90 ± 0.47	$2.19 \cdot 10^{33} \pm 9.70 \cdot 10^{31}$	$2.06 \cdot 10^{36} \pm 1.33 \cdot 10^{36}$	$1.13 \cdot 10^{30} \pm 5.36 \cdot 10^{29}$
Hyades	3750	3999	5	25	665 ± 70	0.13 ± 0.01	$6.3 \cdot 10^{31}$	1.47 ± 0.23	1.45 ± 0.19	$2.12 \cdot 10^{33} \pm 9.71 \cdot 10^{31}$	$5.41 \cdot 10^{15} \pm 1.24 \cdot 10^{15}$	$1.02 \cdot 10^{15} \pm 2.01 \cdot 10^{14}$
Hyades	5000	5999	11	11	665 ± 70	0.13 ± 0.01	$1.9 \cdot 10^{33}$	-	1.06 ± 0.28	$7.75 \cdot 10^{34} \pm 7.76 \cdot 10^{33}$	-	$1.36 \cdot 10^0 \pm 4.59 \cdot 10^{-1}$
Hyades	3500	3749	14	31	665 ± 70	0.13 ± 0.01	$8.8 \cdot 10^{31}$	1.13 ± 0.24	1.16 ± 0.20	$1.54 \cdot 10^{33} \pm 2.27 \cdot 10^{32}$	$2.29 \cdot 10^3 \pm 5.82 \cdot 10^2$	$2.38 \cdot 10^4 \pm 5.14 \cdot 10^3$

Table 3. Summary of activity parameters of all clusters and T_{eff} bins in equivalent duration distributions.

cluster	$T_{\text{min}} [\text{K}]$	$T_{\text{max}} [\text{K}]$	n_*	n_{flares}	age [Myr]	[Fe/H]	$ED_{\text{min}} [\text{s}]$	α_B	α_{MK}	$\beta_2 [\text{yr}^{-1}]$	$\beta_B [\text{yr}^{-1}]$	$\beta_{\text{MK}} [\text{yr}^{-1}]$	tr_2	tr_B	tr_{MK}	
Pleiades	4000	4999	87	110	$125 \pm^{25}_{25}$	-	-0.02 ± 0.03	$2.3 \cdot 10^1$	1.68 ± 0.07	175.40 ± 3.06	26.23 ± 1.80	26.08 ± 1.74	0	0	0	
Pleiades	3000	3249	353	129	$125 \pm^{25}_{25}$	-	-0.02 ± 0.03	$9.1 \cdot 10^2$	2.26 ± 0.12	2.24 ± 0.12	1663.97 ± 8.43	16801.52 ± 1988.56	14323.95 ± 1675.01	0	0	0
Pleiades	3250	3499	168	185	$125 \pm^{25}_{25}$	-	-0.02 ± 0.03	$2.2 \cdot 10^2$	2.03 ± 0.09	2.02 ± 0.09	1250.16 ± 3.32	1524.74 ± 130.65	1437.66 ± 122.52	0	0	0
Pleiades	2500	2999	63	28	$125 \pm^{25}_{25}$	-	-0.02 ± 0.03	$2 \cdot 10^2$	1.40 ± 0.32	1.38 ± 0.26	732.64 ± 89.39	3.07 ± 0.97	2.55 ± 0.68	0	1	1
Pleiades	3750	3999	52	61	$125 \pm^{25}_{25}$	-	-0.02 ± 0.03	$4.6 \cdot 10^1$	1.86 ± 0.12	1.84 ± 0.11	337.15 ± 3.77	133.53 ± 15.57	118.85 ± 13.38	0	0	0
Pleiades	5000	5999	53	14	$125 \pm^{25}_{25}$	-	-0.02 ± 0.03	4.9	1.27 ± 0.25	1.32 ± 0.17	9.24 ± 1.16	0.13 ± 0.03	0.20 ± 0.04	1	1	1
Pleiades	3500	3749	50	47	$125 \pm^{25}_{25}$	-	-0.02 ± 0.03	$1.6 \cdot 10^2$	1.88 ± 0.11	1.84 ± 0.11	838.25 ± 8.01	338.29 ± 38.96	256.41 ± 28.27	0	0	0
M35	4000	4999	221	7	$149 \pm^{13}_{13}$	-	-0.21 ± 0.06	$5.2 \cdot 10^2$	-	1.34 ± 0.76	202.70 ± 21.23	-	0.26 ± 0.20	1	0	1
Rup 147	5000	5999	39	7	$2301 \pm^{380}_{257}$	-	0.08 ± 0.04	4.0	-	1.95 ± 0.30	3.07 ± 0.21	-	2.58 ± 0.79	0	0	0
Hyades	4000	4999	32	22	$665 \pm^{76}_{76}$	-	0.13 ± 0.01	4.4	-	1.13 ± 0.25	30.87 ± 8.30	-	0.05 ± 0.01	0	0	1
Hyades	3000	3249	56	14	$665 \pm^{70}_{70}$	-	0.13 ± 0.01	$9.8 \cdot 10^2$	1.87 ± 0.60	1.78 ± 0.48	1037.31 ± 28.99	316.11 ± 191.27	132.35 ± 63.88	0	1	1
Hyades	3250	3499	42	20	$665 \pm^{70}_{70}$	-	0.13 ± 0.01	$5.5 \cdot 10^2$	1.82 ± 0.37	1.77 ± 0.30	1281.92 ± 18.75	264.94 ± 97.28	156.31 ± 46.78	0	1	1
Hyades	3750	3999	5	21	$665 \pm^{70}_{70}$	-	0.13 ± 0.01	3.9	1.46 ± 0.29	1.49 ± 0.27	157.65 ± 8.25	8.37 ± 2.48	10.09 ± 2.71	0	1	1
Hyades	5000	5999	11	8	$665 \pm^{70}_{70}$	-	0.13 ± 0.01	$2.4 \cdot 10^1$	-	1.06 ± 0.28	182.82 ± 18.30	-	0.01 ± 0.00	1	0	1
Hyades	3500	3749	14	30	$665 \pm^{70}_{70}$	-	0.13 ± 0.01	6.5	-	1.14 ± 0.16	172.86 ± 33.54	-	0.18 ± 0.03	0	0	1

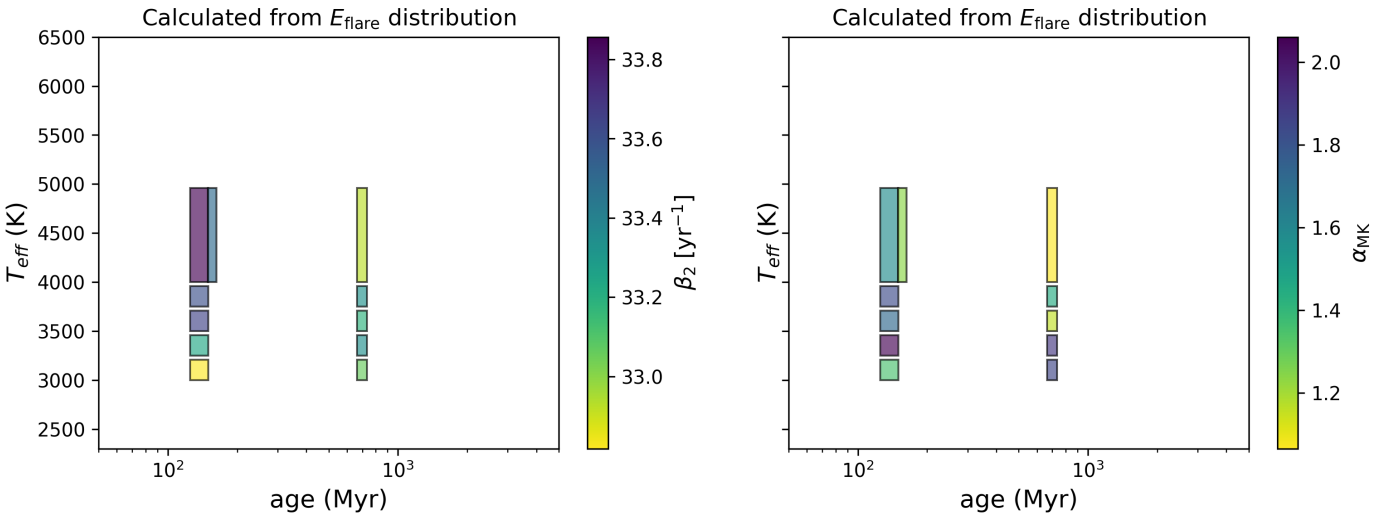


Fig. 12. Power law fit parameters in energy distributions. Left panel: Power law intercept β_2 . Right panel: Power law exponent α_{MK} , fitting procedure follows Mascherger and Kroupa (2009). See Fig. 4 for details on the overall figure layout.

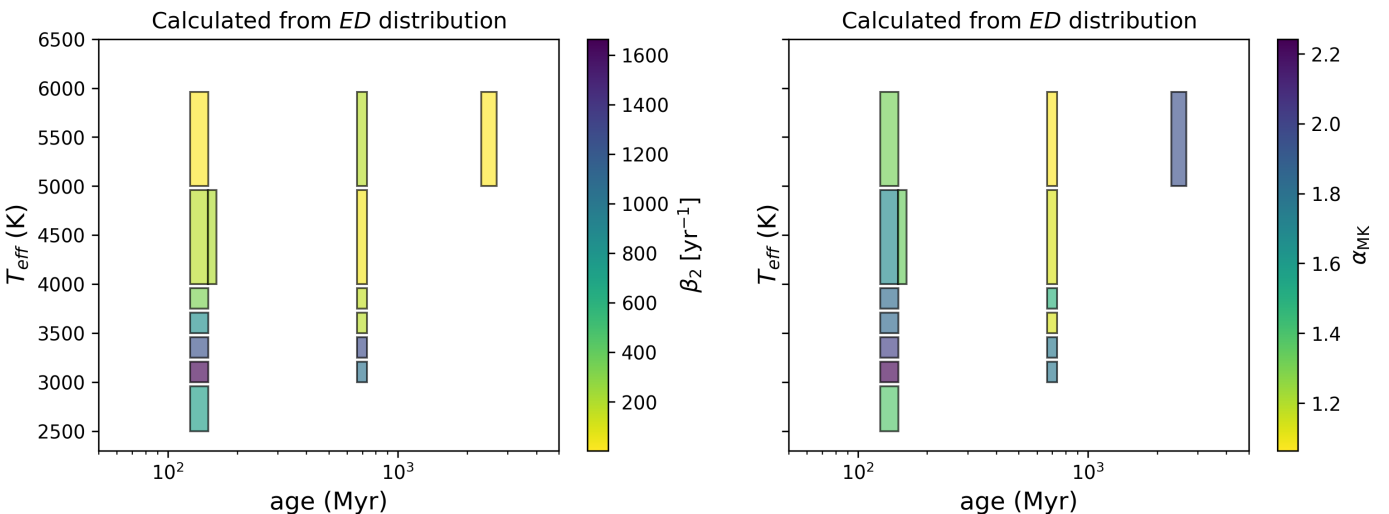


Fig. 13. Power law fit parameters in ED distributions. Left panel: Power law intercept β_2 . Right panel: Power law exponent α_{MK} , fitting procedure follows Mascherger and Kroupa (2009). See Fig. 4 for details on the overall figure layout.

433 et al. 2019) could not be reproduced here or in the EvryFlare 433 survey (Howard et al. 2019b). If enhanced flaring can be interpreted as an increase in the stellar angular momentum loss rate 434 flaring activity can be used to inform the cause of variation in the 435 spin-down efficiency. An example of such variations is the apparent 436 temporary stalling of spin-down seen in K dwarfs in NGC 437 6811 (Curtis+2019). The authors favored a scenario in which 438 the stellar core transfers momentum onto the envelope but did not rule out the possibility of a decreased magnetic braking efficiency. In the latter scenario, these stars should flare less. 441 We used rotation periods derived from K2 light curves for the 442 Pleiades (Rebull et al. 2016b), the Hyades (Douglas et al. 2016), 443 and Praesepe (Rebull et al. 2017), to illuminate the rotation 444 flaring relation at fixed ages. In the Pleiades, most flaring stars 445 are found on the fast rotator branch at or below one day, and 446 flaring activity peaks in this regime. For Praesepe, flaring rates 447 appear to [...] In the Hyades, all of the 11 stars with rotation 448 periods that overlapped with our sample were found flaring, but 449 the number were too low to provide statistical insight. For Rup 450 147, M35 and M67, no rotation rates were available at the time 451 452 453 454 455 456 457 458 459 460 461 462 463 464 465 466 467 468 469

5.2. M37

Comparing our results to a similar study of photometric flares in M37 (Chang et al. 2015) we find the results somewhat discrepant. M37 is 300–600 Myr old and appears less active than Praesepe and Hyades in individual Teff bins, which are of coeval or older. We attribute the difference to the loose membership requirement of $pmem \geq 0.2$ in Chang et al. (2015) as compared to our stricter cuts at 0.8. We expect the M37 to be contaminated with field stars that systematically reduce the flaring rates. Applying our own restriction the M37 sample (Chang et al. 2016) leaves very few flares that hamper a statistical description of their distributions.

5.3. Division at 3000 K

The lowest T_{eff} bin at Pleiades age in our sample reflects the division between fully convective stars and those with a radiative core (Reid & Hawley 2005). At this age, the coolest dwarfs may still be accreting angular momentum on the PMS, instead

470 of spinning down on the MS. We suggest that a regime change⁵²⁵
 471 occurs around 120 Myr for stars with $T_{\text{eff}} = 2500 - 3250$ K.⁵²⁶
 472 Below 3000 K, an analysis of 66 ZDI maps show that magnetic⁵²⁷
 473 field configurations can be strong and dipolar or weak and more⁵²⁸
 474 tipolar (Morin et al. 2008; See et al. 2017). If these stars can be
 475 distinguished by age, this should be reflected in our age-resolved
 476 flaring activity. If the difference is not a function of age, we
 477 should see a similar bimodal distribution of very inactive and
 478 very active stars in the lowest mass bins. If the difference⁵²⁹
 479 between the two configurations is a function of age, we should⁵³⁰
 480 see one type of stars with correspondingly similar behaviour⁵³¹
 481 these T_{eff} bins.⁵³²

482 The lowest mass bin appears underactive compared to the rest⁵³³
 483 in the flaring-age- T_{eff} relation in the ED domain. Physical explana⁵³⁴
 484 tions for this peculiarity include: A different magnetic structure⁵³⁵
 485 A truncation of the power law that reflects the maximum ED ⁵³⁶
 486 active region can produce on these stars.⁵³⁷

487 West et al. (2015) found that all M1-M4 dwarfs with rotation pe⁵³⁸
 488 riods shorter than 26 days, and all M5-M8 dwarfs with periods⁵³⁹
 489 shorter than 86 days show H α emission, indicating their mag⁵⁴⁰
 490 netic activity.⁵⁴¹

491 Assuming a typical binary fraction for early and mid M⁵⁴²
 492 dwarfs (Fischer & Marcy 1992), we can expect some of the flares⁵⁴³
 493 on stars at $T_{\text{eff}} > 3000$ K to belong to unresolved binary com⁵⁴⁴
 494 panions with $T_{\text{eff}} < 3000$ K. A misattributed flare on an early M⁵⁴⁵
 495 dwarf then will be assigned a too small ED , but still a correc⁵⁴⁶
 496 $E_{Kp,\text{flare}}$ because the count ratios are equal to the L_{Kp} ratios.⁵⁴⁷

497 5.4. Consistency of Hyades' and Praesepe's results

498 HRDs constructed in Gaia Collaboration et al. (2018a) indicate⁵⁴⁸
 499 very similar ages for Hyades and Praesepe. We expect our⁵⁴⁹
 500 results to reflect this similarity.⁵⁵⁰

501 Are the samples comparable? Membership determination me⁵⁵¹
 502 differ. Can we frame this as a statistical test, i.e. answer the⁵⁵²
 503 question: What is the probability that the activity distribution⁵⁵³
 504 for both clusters were drawn from the same underlying distribu⁵⁵⁴
 505 tion for a given age and mass bin?⁵⁵⁵

506 Metallicity is controlled for ([Fe/H](Praesepe) = 0.560
 507 [Fe/H](Hyades) = 0.13, Netopil et al. 2016).

508 5.5. Consistency of Pleiades and M35 results

509 M35 is has subsolar metallicity, while Pleiades are roughly solar.⁵⁶⁶

510 5.6. Jim's section(s)

511 Flaring activity function of mass and age – a gyrochronology⁵⁶⁸
 512 analog?⁵⁶⁹

513 Results in the context of Davenport et al. (2019): How well does⁵⁷⁰
 514 the model fit if we have isochronal and not rotational ages⁵⁷¹
 515 for our stars?⁵⁷²

516 Davenport et al. (2019) note a sample bias towards more active⁵⁷³
 517 stars. Their models overpredicts the superflaring rate of the erage⁵⁷⁴
 518 Sun-like sample from Shibayama et al. (2013) and more⁵⁷⁵
 519 resembles the rate for their most active sub-sample. Do we see⁵⁷⁶
 520 the same effect in our OC sample? We should not. Our cluster⁵⁷⁷
 521 memberships depend on activity.⁵⁷⁸

522 5.7. Universality of α

523 Takin into account uncertainties and systematic errors resulting⁵⁸⁵
 524 power law fitting methods, the power law exponent $\alpha \sim 2$ ⁵⁸⁶

525 pears to be constant for all studies on flare statistics so far, ir-
 526 respective of spectral type. A noteable exception are A stars in
 527 Kepler that follow a power law with $\alpha \sim 1$ that may indicate a
 528 different physical process (Yang & Liu 2019).

5.8. Deviations from single power law

Spots can survive on the stellar surface from a few days to nearly a year (Namekata et al. 2017; Davenport 2015). Namekata et al. (2017) find conceivable that spots evolve on timescale shorter than the estimated lifetimes. Complex spot geometry is correlated with the strongest X-class flares on the Sun (Toriumi et al. 2017; Sammis et al. 2000). This support the idea that flares are associated with the presence of certain types of starspots, or more generally, certain types of active regions. Since we can reasonable expect that there is a maximum flare energy a spot can produce, the underlying power law relation must break a some ED_{max} . We tested a possible truncation of our FFDs, but find no conclusive evidence for it in any FFD with > 50 data points. As we stack multiple targets, each potentially with multiple, evolving spots of various sizes on their surfaces, into one FFD at a time, we might observe a deviation but no truncation. A different explanation is simply that we do not sample the maximum energies, as extremely high relative fluxes have been observed in the past (Paudel et al. 2018; Jackman et al. 2019; Schmidt et al. 2016).

6. Summary and Conclusions

Is there or will be there more data available to further extend the sample?

Acknowledgements. This work made use of the `gaia-kepler.fun` crossmatch database created by Megan Bedell. Kepler-affiliated tools were used in the process: `lightkurve`, `K2SC`, `AltaiPony`. Also: `numpy`, `pandas`, `astroML`, `astropy`, `specmatch-emp`, `bokeh` (Bokeh Development Team 2019)... `TOPCAT`: This research made use of the cross-match service provided by CDS, Strasbourg. This work has made use of data from the European Space Agency (ESA) mission `Gaia` (<https://www.cosmos.esa.int/gaia>), processed by the `Gaia` Data Processing and Analysis Consortium (DPAC, <https://www.cosmos.esa.int/web/gaia/dpac/consortium>). Funding for the DPAC has been provided by national institutions, in particular the institutions participating in the `Gaia` Multilateral Agreement. If you have used `Gaia` DR2 data in your research, please cite both the `Gaia` mission paper and the `Gaia` DR2 release paper: Gaia Collaboration et al. (2016): Description of the `Gaia` mission (spacecraft, instruments, survey and measurement principles, and operations), Gaia Collaboration et al. (2018b): Summary of the contents and survey properties.

References

- Aarnio, A. N., Matt, S. P., & Stassun, K. G. 2012, *ApJ*, 760, 9
- Aarnio, A. N., Stassun, K. G., Hughes, W. J., & McGregor, S. L. 2011, *Sol. Phys.*, 268, 195
- Aigrain, S., Parviainen, H., & Pope, B. J. S. 2016, *MNRAS*, 459, 2408
- Alvarado-Gómez, J. D., Drake, J. J., Cohen, O., Moschou, S. P., & Garraffo, C. 2018, *ApJ*, 862, 93
- Andrae, R., Fouesneau, M., Creevey, O., et al. 2018, *A&A*, 616, A8
- Barentsen, G., Hedges, C., Saunders, N., et al. 2018, arXiv e-prints, arXiv:1810.12554
- Barnes, S. A. 2003, *ApJ*, 586, 464
- Bauke, H. 2007, *European Physical Journal B*, 58, 167
- Bessell, M. S. & Brett, J. M. 1988, *Publications of the Astronomical Society of the Pacific*, 100, 1134
- Bokeh Development Team. 2019, Bokeh: Python library for interactive visualization
- Bouy, H., Bertin, E., Barrado, D., et al. 2015, *Astronomy and Astrophysics*, 575, A120
- Boyajian, T. S., von Braun, K., van Belle, G., et al. 2013, *The Astrophysical Journal*, 771, 40

- 587 Candelaresi, S., Hillier, A., Maehara, H., Brandenburg, A., & Shibata, K. 2005
 588 ApJ, 792, 67 666
- 589 Cantat-Gaudin, T., Jordi, C., Vallenari, A., et al. 2018, A&A, 618, A93 667
- 590 Carpenter, J. M. 2001, The Astronomical Journal, 121, 2851 668
- 591 Chambers, K. C., Magnier, E. A., Metcalfe, N., et al. 2016, ArXiv e-prints [arXiv:1612.05560] 670
- 592 Chang, S.-W., Byun, Y.-I., & Hartman, J. D. 2015, ApJ, 814, 35 671
- 593 Chang, S. W., Byun, Y. I., & Hartman, J. D. 2016, VizieR Online Data Catalogue [J/ApJ/814/35] 672
- 594 Clarke, R. W., Davenport, J. R. A., Covey, K. R., & Baranec, C. 2018, ApJ, 857, 59 673
- 595 Curtis, J. L., Wolfgang, A., Wright, J. T., Brewer, J. M., & Johnson, J. A. 2007, AJ, 145, 134 675
- 596 Davenport, J. 2015, PhD thesis, University of Washington 677
- 597 Davenport, J. R. A., Covey, K. R., Clarke, R. W., et al. 2019, ApJ, 871, 241 678
- 598 Davenport, J. R. A., Hawley, S. L., Hebb, L., et al. 2014, ApJ, 797, 122 680
- 599 Doorsselaere, T. V., Shariati, H., & Debosscher, J. 2017, ApJS, 232, 26 681
- 600 Douglas, S. T., Agüeros, M. A., Covey, K. R., et al. 2014, ApJ, 795, 161 682
- 601 Douglas, S. T., Agüeros, M. A., Covey, K. R., et al. 2016, ApJ, 822, 47 683
- 602 Douglas, S. T., Agüeros, M. A., Covey, K. R., & Kraus, A. 2017, ApJ, 842, 884 684
- 603 Drake, J. J., Cohen, O., Yashiro, S., & Gopalswamy, N. 2013, ApJ, 764, 170685
- 604 Finkbeiner, D. P., Schlafly, E. F., Schlegel, D. J., et al. 2016, ApJ, 822, 66 686
- 605 Fischer, D. A. & Marcy, G. W. 1992, ApJ, 396, 178 687
- 606 Froning, C. S., Kowalski, A., France, K., et al. 2019, ApJ, 871, L26 688
- 607 Gaia Collaboration, Babusiaux, C., van Leeuwen, F., et al. 2018a, A&A, 619, A10 690
- 608 Gaia Collaboration, Brown, A. G. A., Vallenari, A., et al. 2018b, A&A, 616, 601 691
- 609 Gao, X. 2018, ApJ, 869, 9 692
- 610 Gao, X. 2018, The Astrophysical Journal, 869, 9 693
- 611 Gizon, J. E. 2013, ApJ, 779, 172 694
- 612 Gonzalez, G. 2016, MNRAS, 459, 1060 695
- 613 Green, G. M., Schlafly, E. F., Finkbeiner, D., et al. 2018, MNRAS, 478, 651 696
- 614 Green, G. M., Schlafly, E. F., Zucker, C., Speagle, J. S., & Finkbeiner, D. P. 2019, arXiv e-prints, arXiv:1905.02734 697
- 615 Hawley, S. L. & Fisher, G. H. 1992, ApJS, 78, 565
- 616 Hilton, E. J., West, A. A., Hawley, S. L., & Kowalski, A. F. 2010, AJ, 140, 1402
- 617 Howard, W. S., Corbett, H., Law, N. M., et al. 2019a, ApJ, 881, 9
- 618 Howard, W. S., Corbett, H., Law, N. M., et al. 2019b, arXiv e-prints, arXiv:1907.10735
- 619 Howell, S. B., Sobeck, C., Haas, M., et al. 2014, PASP, 126, 398
- 620 Hunt-Walker, N. M., Hilton, E. J., Kowalski, A. F., Hawley, S. L., & Matthews, J. M. 2012, PASP, 124, 545
- 621 Ilin, E., Schmidt, S. J., Davenport, J. R. A., & Strassmeier, K. G. 2019, A&A, 622, A133
- 622 Jackman, J. A. G., Wheatley, P. J., Bayliss, D., et al. 2019, arXiv e-prints, arXiv:1902.00900
- 623 Kerr, G. S. & Fletcher, L. 2014, ApJ, 783, 98
- 624 Kleint, L., Heinzel, P., Judge, P., & Krucker, S. 2016, ApJ, 816, 88
- 625 Koch, D. G., Borucki, W. J., Basri, G., et al. 2010, ApJ, 713, L79
- 626 Kovács, G., Bakos, G., & Noyes, R. W. 2005, MNRAS, 356, 557
- 627 Kowalski, A. F., Hawley, S. L., Wisniewski, J. P., et al. 2013, ApJS, 207, 15
- 628 Kretzschmar, M. 2011, A&A, 530, A84
- 629 Lecavelier des Etangs, A., Bourrier, V., Wheatley, P. J., et al. 2012, A&A, 543, L4
- 630 Loyd, R. O. P., France, K., Youngblood, A., et al. 2018, ApJ, 867, 71
- 631 Luger, R., Kruse, E., Foreman-Mackey, D., Agol, E., & Saunders, N. 2018, AJ, 156, 99
- 632 Lurie, J. C., Davenport, J. R. A., Hawley, S. L., et al. 2015, ApJ, 800, 95
- 633 Mann, A. W., Feiden, G. A., Gaidos, E., Boyajian, T., & von Braun, K. 2015, ApJ, 804, 64
- 634 Mann, A. W., Feiden, G. A., Gaidos, E., Boyajian, T., & von Braun, K. 2016, The Astrophysical Journal, 819, 87
- 635 Maschberger, T. & Kroupa, P. 2009, MNRAS, 395, 931
- 636 Mondrik, N., Newton, E., Charbonneau, D., & Irwin, J. 2019, ApJ, 870, 10
- 637 Morin, J., Donati, J. F., Petit, P., et al. 2008, MNRAS, 390, 567
- 638 Namekata, K., Sakaue, T., Watanabe, K., et al. 2017, ApJ, 851, 91
- 639 Nardiello, D., Libralato, M., Bedin, L. R., et al. 2016, MNRAS, 463, 1831
- 640 Olivares, J., Bouy, H., Sarro, L. M., et al. 2019, A&A, 625, A115
- 641 Olivares, J., Sarro, L. M., Moraux, E., et al. 2018, A&A, 617, A15
- 642 Paudel, R. R., Gizon, J. E., Mullan, D. J., et al. 2018, ApJ, 861, 76
- 643 Pecaut, M. J. & Mamajek, E. E. 2013, ApJS, 208, 9
- 644 Priest, E. & Forbes, T. 2002, A&A Rev., 10, 313
- 645 Rebull, L., Stauffer, J., Bouvier, J., et al. 2016a, Astronomical Journal, 152, 113, bibtext: 2016AJ....152..113R bib-
 646 tex[eid=113;adsurl=https://ui.adsabs.harvard.edu/abs/2016AJ....152..113R;adsnote=Provided
 647 by the SAO/NASA Astrophysics Data System]
- 648 Rebull, L. M., Stauffer, J. R., Bouvier, J., et al. 2016b, AJ, 152, 113
- 649 Rebull, L. M., Stauffer, J. R., Hillenbrand, L. A., et al. 2017, ApJ, 839, 92
- 650 Reid, I. N. & Hawley, S. L. 2005, New Light on Dark Stars: Red Dwarfs, Low-Mass Stars, Brown Dwarfs, 2nd edn., Springer-Praxis books in astronomy and astrophysics (Berlin ; New York : Chichester, UK: Springer ; Praxis)
- 651 Reino, S., de Bruijne, J., Zari, E., d'Antona, F., & Ventura, P. 2018, MNRAS, 477, 3197
- 652 Sammis, I., Tang, F., & Zirin, H. 2000, ApJ, 540, 583
- 653 Schmidt, S. J., Shappee, B. J., Gagné, J., et al. 2016, ApJ, 828, L22
- 654 See, V., Jardine, M., Vidotto, A. A., et al. 2017, MNRAS, 466, 1542
- 655 Shibayama, T., Maehara, H., Notsu, S., et al. 2013, The Astrophysical Journal Supplement Series, 209, 5
- 656 Shibayama, T., Maehara, H., Notsu, S., et al. 2013, ApJS, 209, 5
- 657 Skrutskie, M. F., Cutri, R. M., Stiening, R., et al. 2006, AJ, 131, 1163
- 658 Soares-Furtado, M., Hartman, J. D., Bakos, G. Á., et al. 2017, Publications of the Astronomical Society of the Pacific, 129, 044501
- 659 Tilley, M. A., Segura, A., Meadows, V., Hawley, S., & Davenport, J. 2019, Astrobiology, 19, 64
- 660 Toriumi, S., Schrijver, C. J., Harra, L. K., Hudson, H., & Nagashima, K. 2017, ApJ, 834, 56
- 661 Van Cleve, J. E., Howell, S. B., Smith, J. C., et al. 2016, PASP, 128, 075002
- 662 Vanderburg, A. & Johnson, J. A. 2014, Publications of the Astronomical Society of the Pacific, 126, 948
- 663 Vanderplas, J., Connolly, A., Ivezić, Ž., & Gray, A. 2012, in Conference on Intelligent Data Understanding (CIDU), 47–54
- 664 Vinícius, Z., Barentsen, G., Hedges, C., Gully-Santiago, M., & Cody, A. M. 2018
- 665 Watanabe, K., Shimizu, T., Masuda, S., Ichimoto, K., & Ohno, M. 2013, ApJ, 776, 123
- 666 West, A. A., Weisenburger, K. L., Irwin, J., et al. 2015, ApJ, 812, 3
- 667 Wheatland, M. S. 2004, ApJ, 609, 1134
- 668 Yang, H. & Liu, J. 2019, ApJS, 241, 29
- 669 Yang, H., Liu, J., Gao, Q., et al. 2017, ApJ, 849, 36
- 670 Yang, H., Liu, J., Qiao, E., et al. 2018, ApJ, 859, 87
- 671 Yee, S. W., Petigura, E. A., & von Braun, K. 2017, ApJ, 836, 77

697 Appendix A: Membership probabilities

698 To match catalogs on RA and declination we used `astroML.crossmatch` tool for Python (Vanderplas et al. 2012)
 699 For the studies with classifiers we assigned membership proba
 700 bilities as follows. In Gonzalez (2016):
 701

$$\begin{aligned} p(M(\text{member})) &= 0.9, \\ p(BM(\text{binary member})) &= 0.9, \\ p(N(\text{non-member})) &= 0.1, \\ p(SN(\text{single non-member})) &= 0.1, \\ p(BN(\text{binary non-member})) &= 0.1, \\ p(U(\text{unknown member})) &= 0.5. \end{aligned}$$

702 In Curtis et al. (2013):

$$\begin{aligned} p(Y(\text{highest confidence member})) &= 0.9, \\ p(P(\text{possible/probable member})) &= 0.7, \\ p(N(\text{not likely/non-member})) &= 0.7, \\ p(B(\text{photometry consistent with blue stragglers})) &= 0.0. \end{aligned}$$

703 In Rebull et al. (2017):

$$\begin{aligned} p((\text{best})) &= 0.9, \\ p((\text{ok})) &= 0.6, \\ p((\text{else})) &= 0.1. \end{aligned}$$

704 Members from Rebull et al. (2016a); Douglas et al. (2017); and
 705 Gaia Collaboration et al. (2018a) were assigned $p = 0.9$ if they
 706 appeared in the final catalog.
 707 Table A.1 gives an overview over different membership catalogues.
 708 Figure A.1 shows membership probability histograms of the final sample broken down by membership source. Detailed instructions on how to reproduce the final sample of members in each cluster, and corresponding tables, Python scripts, and Jupyter notebooks can be found online⁵

713 Appendix B: Cluster parameters

714 Appendix C: Broadband photometry: quality cuts
 715 and conversions

716 We required `flux/flux_error` ≥ 10 for Gaia G, BP, and RP bands. We require that the 2MASS measurements for J, H, and K to be "A". "A" means that measurements had $S/N > 10$ and $\sigma < 0.11$. For PanSTARRS photometry, we required that the QF_OBJ_GOOD quality filter flag was set.
 721 SDSS and PS1 *ugrizy* bands are similar but not identical, but can be converted using Table 2 in Finkbeiner et al. (2016).

723 Appendix D: Pixel saturation

724 Resolve different levels of pixel saturation (>1 , >10) and how
 725 they contribute to the deviations from the single power law at
 726 the highest energies.

⁵ <https://github.com/ekaterinailin/flares-in-clusters-with-k2-ii>

727 Appendix E: Solar system objects

728 Solar system objects (SSOs) produce brightness excursions in
 729 K2 light curves that can closely resemble flare signatures. Often,
 730 they can be distinguished by their symmetric rise and decay
 731 shape as contrasted with the typical fast-rise gradual decay flare
 732 shape (Davenport et al. 2014). M. H. Christiansen and colleagues
 733 developed a routine called SkyBoT that matches positions and
 734 times to passages of SSOs listed in YYY. RA, declination, start,
 735 stop, and mid epochs of flares in BKJD are the input parameters.
 736 We excluded all flare candidates that occurred within X minutes
 737 of a SSO passage at the star's position. This procedure removed
 738 ZZ% of all flare candidates. In the case of high energy flares, we
 739 confirmed the passage by manually inspecting the pixel file with
 740 the `lightkurve.interact` function for TargetPixelFiles.

741 Appendix F: Universality of power law exponent α

742 We compiled a exhaustive (?) table of previous work where
 743 power laws were fitted to FFDs using different methods. Table
 744 F.1 lists the overview. While particular studies consistently find
 745 values above or below $\alpha \approx 2$, the comparison of different studies
 746 points towards unresolved systematic errors in all these studies.

747 Appendix G: Expanding the likelihood

The rate λ_2 of flares with energies larger than S_2 is given in Wheatland (2004) as

$$\lambda_2 = \lambda_1 \cdot \left(\frac{S_1}{S_2} \right)^{\alpha-1}. \quad (\text{G.1})$$

S_1 denotes the energy above which all flares are detected. λ_1 is the corresponding rate. α remains the power law exponent of the flare frequency distribution.

We are also given the posterior distribution for the rate λ_2 of flares above S_2 in Eq. (20) in Wheatland (2004):

$$\begin{aligned} P_2(\lambda_2) &= \int_1^\infty d\alpha \int_0^\infty d\lambda_1 \delta\left(\lambda_2 - \lambda_1 \cdot \left(\frac{S_1}{S_2} \right)^{\alpha-1}\right) \\ &\quad \cdot P_1(\lambda_1) \cdot P_\alpha(\alpha) \end{aligned} \quad (\text{G.2})$$

As we have additional information in the form of uncertainties in our data $S = \{S_i, \lambda_i, \sigma_{S,i}\}$, we can expand Eq. G.2 with this knowledge. Assuming that the observed flare energies S_i with cumulative rates λ_i are distributed around the real flare energies $S_{0,i}$ with Gaussian uncertainties $\sigma_{S,i}$, we can define:

$$\begin{aligned} p(S_i|\lambda_1, \alpha, \sigma_{S,i}) &= \frac{1}{2\pi\sqrt{\sigma_{S,i}}} e^{-\frac{(S_i - S_{0,i})^2}{2\sigma_{S,i}^2}} \\ &\quad - \frac{\left(S_i - S_1 \left(\frac{\lambda_i}{\lambda_1} \right)^{-1/(\alpha-1)} \right)^2}{2\sigma_{S,i}^2} \end{aligned} \quad (\text{G.3})$$

We assume in Eq. G.3 that uncertainties on λ_1 are negligible. Eq. G.2 then reads:

$$\begin{aligned} P_2(\lambda_2) &= \int_1^\infty d\alpha \int_0^\infty d\lambda_1 \delta\left(\lambda_2 - \lambda_1 \cdot \left(\frac{S_1}{S_2} \right)^{\alpha-1}\right) \\ &\quad \cdot P_1(\lambda_1) \cdot P_\alpha(\alpha) \cdot P_S(S|\lambda_1, \alpha, \sigma_S) \end{aligned} \quad (\text{G.4})$$

Table A.1. Membership catalogs overview. No distance are given for Hyades we adopted individual distances for all members.

source	type	clusters covered	notes
Curtis et al. (2013)	classifier	Rup 147	
Douglas et al. (2014)	probability	Hyades, Praesepe	meta study
Bouy et al. (2015)	probability	M35	DANCe
Gonzalez (2016)	classifier	M67	
Rebull et al. (2016a)	members list	Pleiades	meta study
Rebull et al. (2017)	classifier	Praesepe	meta study
Douglas et al. (2017)	members list	Praesepe	meta study
Gaia Collaboration et al. (2018a)	members list	Hyades, M35, Rup 147, Pleiades, Praesepe	Gaia DR2, (1)
Cantat-Gaudin et al. (2018)	probability	M35, Rup147, Pleiades, Praesepe	Gaia DR2
Gao (2018)	probability	M67	Gaia DR2
Reino et al. (2018)	probability	Hyades	Gaia DR1, (1)
Olivares et al. (2018)	probability	Pleiades	Gaia DR2, DANCe
Olivares et al. (2019)	probability	Rup 147	Gaia DR2, DANCe

Notes. DANCe: DANCe membership study project. (1) Positions for Hyades were propagated to epoch 2000 using Gaia proper motions.

with

$$P_S(S|\lambda_1, \alpha, \sigma_S) = C \prod_{i=1}^M p(S_i|\lambda_1, \alpha, \sigma_{S,i}). \quad (\text{G.5})$$

760 C absorbs the normalization, or evidence term.

761 Following Wheatland (2004), we marginalize over λ_1 using the
762 δ function in G.4 to obtain

$$\begin{aligned} P_2(\lambda_2) &= \int_1^\infty d\alpha \cdot P_1\left(\lambda_2 \cdot \left(\frac{S_2}{S_1}\right)^{\alpha-1}\right) \cdot P_\alpha(\alpha) \\ &\cdot P_S\left(S|\lambda_2 \cdot \left(\frac{S_2}{S_1}\right)^{\alpha-1}, \alpha, \sigma_S\right) \end{aligned} \quad (\text{G.6})$$

763 Transforming P_S into a function of ϵ with $\lambda_1 = -\ln(1-\epsilon)/\Delta T$
764 yields:

$$\begin{aligned} P_S(S|\epsilon, \alpha, \sigma_S) &= C \prod_{i=1}^M p(S_i|\epsilon, \alpha, \sigma_{S,i}) \\ &= \frac{C}{\Delta T(1-\epsilon)} \\ &\cdot \prod_{i=1}^M \left[\frac{1}{2\pi\sqrt{\sigma_{S,i}}} e^{-\frac{\left(S_i - S_2 \left(\frac{-\ln(1-\epsilon)}{\Delta T\lambda_i}\right)^{1/(\alpha-1)}\right)^2}{2\sigma_{S,i}^2}} \right] \end{aligned} \quad (\text{G.7})$$

765 Finally, P_S enters the joint posterior distribution from Eq. 2, that
766 becomes

$$\begin{aligned} p(\epsilon, \alpha) &= C \cdot (-\ln(1-\epsilon)^M) \\ &\cdot (\alpha-1)^M \cdot \Gamma(\alpha) \left[\frac{(S_2/S_1)^{M+1}}{\pi} \right]^\alpha \\ &\cdot (1-\epsilon)^{(T/\Delta T) \cdot (S_2/S_1)^{\alpha-1}-1} \\ &\cdot P_S(S|\epsilon, \alpha, \sigma_S). \end{aligned} \quad (\text{G.8})$$

767

Table B.1. Non-exhaustive literature overview over OC parameters.

cluster	source	distance [pc]	age [Myr]	[Fe/H]
M35	adopted in this work:	861	$147.5 \pm^{13.5}_{13.5}$	-0.21 ± 0.10
M35	Bossini et al. (2019) ^a		$402.7 \pm^{13.5}_{0.9}$	
M35	Cantat-Gaudin et al. (2018)	861		
M35	Netopil et al. (2016)			-0.21
M35	Scholz et al. (2015)	830	151	
M35	Geller et al. (2010)		133	
M35	Meibom et al. (2009)		$147.5 \pm^{13.5}_{13.5}$	
M35	Bragaglia and Tosi (2006)	912		
M35	Steinhauser and Deliyannis (2004)			-0.143 ± 0.014
M35	Barrado (2001)		180	
M35	Barrado et al. (2001)			-0.21 ± 0.10
M35	Sung and Bessel (1999)	832		
Rup 147	adopted in this work:	305	$2650 \pm^{380}_{380}$	0.08 ± 0.07
Rup 147	Bragaglia et al. (2018)			0.08 ± 0.07
Rup 147	Cantat-Gaudin et al. (2018)	305		
Rup 147	Gaia Collaboration (2018)	309	$1995 \pm^{404}_{257}$	
Rup 147	Torres et al. (2018)	283	$2650 \pm^{380}_{380}$	
Rup 147	Curtis (2016) ^b			0.10 ± 0.02
Rup 147	Scholz et al. (2015)	270	1953	
Rup 147	Curtis et al. (2013)	300	$3125 \pm^{125}_{125}$	0.07 ± 0.03
Pleiades	adopted in this work:	135.6	$135 \pm^{25}_{25}$	-0.037 ± 0.026
Pleiades	Bossini et al. (2019) ^a		$86.5 \pm^{2.4}_{2.4}$	
Pleiades	Cantat-Gaudin et al. (2018)	135.6		
Pleiades	Gossage et al. (2018)		$135 \pm^{25}_{25}$	
Pleiades	Yen et al. (2018)	126.3	$141.3 \pm^{170}_{100}$	
Pleiades	Chelli and Duvert (2016)	139		
Pleiades	Netopil et al. (2016)			-0.01
Pleiades	Dahm (2015)		$112 \pm^{5}_{5}$	
Pleiades	Scholz et al. (2015)	130	120	
Pleiades	Conrad et al. (2014)			-0.037 ± 0.026
Pleiades	Melis et al. (2014)	136		
Pleiades	Bell et al. (2012)	135	125	
Praesepe	adopted in this work:	185.5	$750 \pm^{3}_{3}$	0.16
Praesepe	Bossini et al. (2019)		$750 \pm^{3}_{7}$	
Praesepe	Cantat-Gaudin et al. (2018)	185.5		
Praesepe	Gossage et al. (2018)		590	
Praesepe	Yen et al. (2018)	183	$794 \pm^{253}_{269}$	
Praesepe	Netopil et al. (2016)			0.16
Praesepe	Scholz et al. (2015)	187	832	
Praesepe	Boesgaard et al. (2013)			0.12
Praesepe	Boudreault et al. (2012)	160	630	
Praesepe	Salaris et al. (2004)	175	650	
M67	adopted in this work:	908	$3639 \pm^{17}_{17}$	$-0.102 \pm .081$
M67	Bossini et al. (2019)		$3639 \pm^{17}_{17}$	
M67	Netopil et al. (2016)			0.03
M67	Scholz et al. (2015)		$3428 \pm^{147}_{72}$	
M67	Conrad et al. (2014)			$-0.102 \pm .081$
M67	Dias et al. (2012)	908	4300	
M67	Oñehag et al. (2011)	880	4200	0.02
Hyades	adopted in this work: ^c		$690 \pm^{160}_{100}$	0.13 ± 0.02
Hyades	Gaia Collaboration (2018)		$690 \pm^{160}_{100}$	
Hyades	Gossage et al. (2018)		680	
Hyades	Liu et al. (2016)			± 0.02
Hyades	Netopil et al. (2016)			0.13
Hyades	Taylor and Joner (2005)			0.103 ± 0.008
Hyades	Cummings et al. (2005)			0.146 ± 0.004
Hyades	Salaris et al. (2004)		650	0.15
Hyades	Perryman et al. (1998)		$625 \pm^{50}_{50}$	
Hyades	Martin et al. (1998)		$650 \pm^{70}_{70}$	

Article number, page 20 of 22
Notes. ^(a) Bossini et al. (2019) noted some caveats for their determination of ages of young clusters, for which they used Gaia DR2 photometry for isochrone fitting. ^(b) Curtis (2016) reanalysed HIRES spectra using an improved spectroscopic method as compared to Curtis et al. (2013). ^(c) We did not adopt a mean value for the Hyades distance because the cluster members are on average closer than 50 pc.

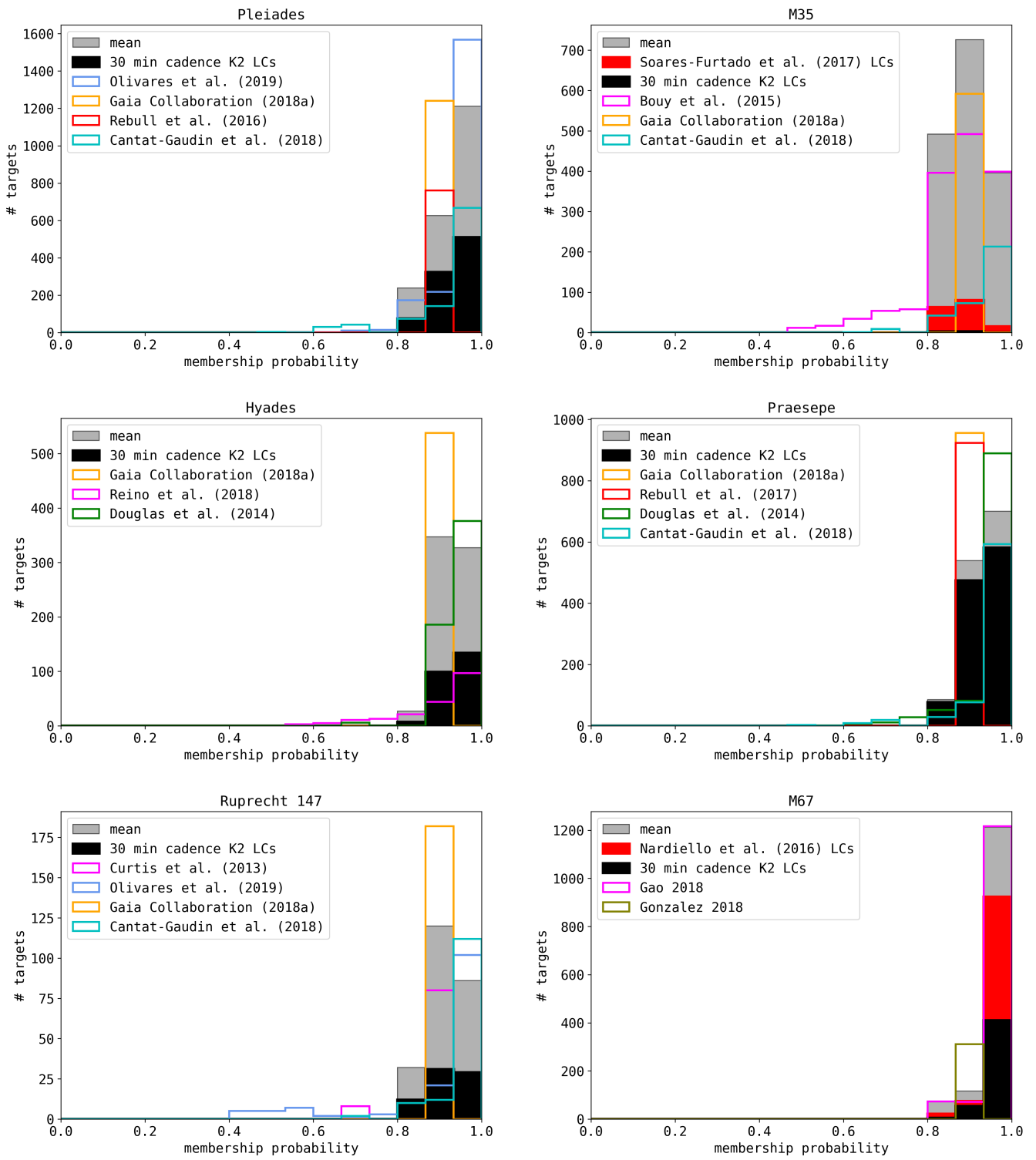


Fig. A.1. Membership histograms.

Table F.1. Literature overview over power law fitting approaches to FFDs.

Who	method	data	$\alpha - 1$
Hawley et al. (2014)	LSq with Poisson uncertainty, increase the low energy limit until the fit is robust		
Davenport (2016)	weighted LSq, asymmetric Poisson confidence intervals following Gehrels1986		
Gizis (2017)	de-biased MLE (Arnold2015), weight each point with $\text{sqrt}(N)$ in each bin (Clauset+2009)		
Paudel et al. (2018)	ML from a paper in 2010, used emcee (Foreman-Mackey2013)		
Lacy (1976)	graphical, linear LSq	386 flares on UV Cetis	.43-1.
Güdel et al.(2003)	-		
Davenport et al. (2012)	Fit $\log_{10} Y = \alpha + (\beta \log_{10} X)(10 - \gamma/(X + \delta))$	~50,000 M dwarfs from SDSS and 1321 M dwarfs from 2MASS	.9-2.1
Lurie et al. (2015)	Bayesian Markov chain Monte Carlo based algorithm (Kelly 2007) for linear regression	2 dMe5 dwarfs	.92-1.03
Audard et al. (2000)	Crawford+1970 MLE (Jauncey-style)	EUVE 12 F-M type stars, 10-20 flares each	.46-1.61
Shakhovskaia (1989)	linear representation, power laws from Gershberg/Shakhovskaya1983	30-40 dK0-dM8, 200 flares	.4-1.4
Yang et al. (2017)	binned FFDs	103187 flares on 540 M-type dwarfs in Kepler	1.07 +/- 0.35
Howard et al. (2018)			